

Central Lancashire Online Knowledge (CLoK)

Title	An Ammonia Spectral Map of the L1495-B218 Filaments in the Taurus Molecular Cloud: II CCS & HC 7 N Chemistry and Three Modes of Star Formation in the Filaments
Type	Article
URL	https://clock.uclan.ac.uk/id/eprint/28134/
DOI	https://doi.org/10.3847/1538-4357/aaf887
Date	2019
Citation	Seo, Young Min, Majumdar, Liton, Goldsmith, Paul F., Shirley, Yancy L., Willacy, Karen, Ward-Thompson, Derek and Et, Al (2019) An Ammonia Spectral Map of the L1495-B218 Filaments in the Taurus Molecular Cloud: II CCS & HC 7 N Chemistry and Three Modes of Star Formation in the Filaments. <i>The Astrophysical Journal</i> , 871 (134). ISSN 0004-637X
Creators	Seo, Young Min, Majumdar, Liton, Goldsmith, Paul F., Shirley, Yancy L., Willacy, Karen, Ward-Thompson, Derek and Et, Al

It is advisable to refer to the publisher's version if you intend to cite from the work.
<https://doi.org/10.3847/1538-4357/aaf887>

For information about Research at UCLan please go to <http://www.uclan.ac.uk/research/>

All outputs in CLoK are protected by Intellectual Property Rights law, including Copyright law. Copyright, IPR and Moral Rights for the works on this site are retained by the individual authors and/or other copyright owners. Terms and conditions for use of this material are defined in the <http://clock.uclan.ac.uk/policies/>



An Ammonia Spectral Map of the L1495-B218 Filaments in the Taurus Molecular Cloud.

II. CCS and HC₇N Chemistry and Three Modes of Star Formation in the Filaments

Young Min Seo¹, Liton Majumdar¹, Paul F. Goldsmith¹, Yancy L. Shirley², Karen Willacy¹, Derek Ward-Thompson³, Rachel Friesen⁴, David Frayer⁵, Sarah E. Church⁶, Dongwoo Chung⁶, Kieran Cleary⁷, Nichol Cunningham^{5,8}, Kiruthika Devaraj⁶, Dennis Egan⁵, Todd Gaier¹, Rohit Gawande¹, Joshua O. Gundersen⁹, Andrew I. Harris¹⁰, Pekka Kangaslahti¹, Anthony C. S. Readhead⁷, Lorene Samoska¹, Matthew Sieth⁶, Michael Stennes⁵, Patricia Voll⁶, and Steve White⁵

¹ Jet Propulsion Laboratory, California Institute of Technology, 4800 Oak Grove Drive, Pasadena, CA 91109, USA

² Department of Astronomy & Steward Observatory, University of Arizona, 933 N. Cherry Avenue, Tucson, AZ 85721, USA

³ Jeremiah Horrocks Institute, University of Central Lancashire, Preston PR1 2HE, UK

⁴ National Radio Astronomy Observatory, 520 Edgemont Road, Charlottesville, VA 22903, USA

⁵ Green Bank Observatory, 155 Observatory Road, Green Bank, WV 24944, USA

⁶ Kavli Institute for Particle Astrophysics and Cosmology; Physics Department, Stanford University, Stanford, CA 94305, USA

⁷ California Institute of Technology, Pasadena, CA 91125, USA

⁸ Institut de Radioastronomie Millimétrique (IRAM), 300 rue de la Piscine, F-38406 Saint Martin d'Hères, France

⁹ Department of Physics, University of Miami, 1320 Campo Sano Drive, Coral Gables, FL 33146, USA

¹⁰ Department of Astronomy, University of Maryland, College Park, MD 20742, USA

Received 2017 December 21; revised 2018 December 12; accepted 2018 December 13; published 2019 January 28

Abstract

We present deep CCS and HC₇N observations of the L1495-B218 filaments in the Taurus molecular cloud obtained using the *K*-band focal plane array on the 100 m Green Bank Telescope. We observed the L1495-B218 filaments in CCS $J_N = 2_1-1_0$ and HC₇N $J = 21-20$ with a spectral resolution of 0.038 km s^{-1} and an angular resolution of $31''$. We observed strong CCS emission in both evolved and young regions and weak emission in two evolved regions. HC₇N emission is observed only in L1495A-N and L1521D. We find that CCS and HC₇N intensity peaks do not coincide with NH₃ or dust continuum intensity peaks. We also find that the fractional abundance of CCS does not show a clear correlation with the dynamical evolutionary stage of dense cores. Our findings and chemical modeling indicate that the fractional abundances of CCS and HC₇N are sensitive to the initial gas-phase C/O ratio, and they are good tracers of young condensed gas only when the initial C/O is close to solar value. Kinematic analysis using multiple lines, including NH₃, HC₇N, CCS, CO, HCN, and HCO⁺, suggests that there may be three different star formation modes in the L1495-B218 filaments. At the hub of the filaments, L1495A/B7N has formed a stellar cluster with large-scale inward flows (fast mode), whereas L1521D, a core embedded in a filament, is slowly contracting because of its self-gravity (slow mode). There is also one isolated core that appears to be marginally stable and may undergo quasi-static evolution (isolated mode).

Key words: ISM: clouds – ISM: molecules – radio lines: ISM – stars: formation – surveys

1. Introduction

Star formation is one of the fundamental processes in the universe because it drives the evolution of galaxies and sets up the initial conditions for planet formation and the emergence of life. Star formation begins with gravitational contraction of a molecular cloud forming progressively smaller and denser structures, such as molecular filaments and dense cores. If a dense core becomes gravitationally unstable, it forms a protostar or a group of protostars. Although this general framework is established, the details of the star formation processes are still poorly understood. In particular, how a molecular cloud evolves to filaments and dense cores and how dense cores within filaments interact with their surroundings and evolve to form stars are key questions. Answering these questions has been challenging because of difficulties in observations.

The main difficulty originates from making complete and consistent observations toward structures over a wide range of physical properties. Molecular clouds are typically a few tens of parsecs in size, with an average density of 100 cm^{-3} . Molecular cloud cores are less than 0.5 parsecs in size, with central densities ranging from 10^4 cm^{-3} to $>10^6 \text{ cm}^{-3}$. The first hydrostatic cores are expected to be a few astronomical units in size with a density of 10^{10} cm^{-3} and a temperature of 2000 K.

A submillimeter/millimeter-wavelength continuum observation may trace dust structures over a wide range of column densities from a molecular cloud to a first hydrostatic core, but it does not yield any velocity information. On the other hand, molecular lines give velocity information and facilitate identification of complex three-dimensional structures. However, the range of physical properties traced by a single molecular line is firmly limited by the chemical and excitation characteristics of the molecule. Thus, it is crucial to know which physical and chemical condition of complex structures can be correctly traced by a specific molecular line and how to interpret the kinematic information.

In this study, we make observations in CCS $J_N = 2_1-1_0$ toward the L1495-B218 filaments in Taurus. We investigate what CCS $J_N = 2_1-1_0$ is tracing in the region and discuss various modes of star formation in the L1495-B218 filaments using complementary spectral observations of HC₇N, HCN, HCO⁺, and CO isotopologues.

CCS is a carbon-chain molecule that is frequently found in dense cores in nearby, low-mass star-forming clouds (e.g., Suzuki et al. 1992; Wolkovitch et al. 1997; Rathborne et al. 2008; Roy et al. 2011; Marka et al. 2012; Tatematsu et al. 2014b). Yet, what physical and chemical properties of star-forming clouds can be probed by CCS and how CCS traces the chemical evolution

during star formation are still debated. Suzuki et al. (1992) made the first CCS survey toward 49 dense cores in Taurus and Ophiuchus, as well as a chemical evolution model of CCS with respect to the dense gas tracers NH_3 and N_2H^+ . They found that carbon-chain molecules, including CCS and cyanopolyynes (HC_xN ; $x = 3, 5, 7, \dots$), are less abundant in star-forming regions where NH_3 emission is strong. Their chemical model also predicts that the abundance ratio of $[\text{CCS}]/[\text{NH}_3]$ has an anticorrelation with time due to CCS depletion (Suzuki et al. 1992; Aikawa et al. 2001). Some surveys of Bok globules and dense cores supported the chemical model of Suzuki et al. (1992) by showing a trend of low $[\text{CCS}]/[\text{NH}_3]$ ratios in protostellar cores but high $[\text{CCS}]/[\text{NH}_3]$ ratios in starless cores (Scappini et al. 1996; de Gregorio-Monsalvo et al. 2006; Foster et al. 2009; Tatematsu et al. 2014a).

Several observations have results that are not consistent with the chemical model of Suzuki et al. (1992). Benson et al. (1998) found no clear trend of $[\text{CCS}]/[\text{N}_2\text{H}^+]$ as a function of the evolutionary stage of the 20 dense cores with both CCS and N_2H^+ emission in their survey of 60 dense cores. Marka et al. (2012) also showed that the isolated Bok globules in their survey do not have a clear anticorrelation of the $N(\text{CCS})/N(\text{NH}_3)$ ratio with evolutionary state moving from starless cores to protostellar cores. Observations toward infrared dark clouds in NH_3 and CCS using the Robert C. Byrd Green Bank Telescope (GBT) and the Very Large Array do not show any evidence of a trend in $N(\text{CCS})/N(\text{NH}_3)$ from starless to protostellar clumps but rather have highly scattered values (Dirienzo et al. 2015). Furthermore, a quantitative analysis of the fractional abundances of CCS, NH_3 , HCO^+ , CO, and so forth from spatially resolved core observations shows considerably inconsistencies with the prediction of Suzuki et al. and suggests that either the model of chemical processes in a dense core needs to be revised (Lee et al. 2003) or that a dynamically evolving dense core (e.g., a core with infall motion) has a considerably different chemical evolutionary path than that of a static core (Shematovich et al. 2003).

We use the L1495-B218 filaments in Taurus to study the physical and chemical properties of CCS and HC_7N and to investigate the star formation processes in the Taurus molecular cloud using complementary high-resolution observations, including HCN, HCO^+ , and CO isotopologues. The L1495-B218 filaments in Taurus, which consist of multiple velocity-coherent filaments (Hacar et al. 2013), are good test beds because their structures and evolutionary stages are well observed and determined from large to dense core scale. Goldsmith et al. (2008) observed large-scale structures in the Taurus molecular cloud including the L1495-B218 filaments in ^{12}CO and ^{13}CO $J = 1-0$. Their observations also showed that there is a converging or a shear flow toward the filaments (Narayanan et al. 2008; Palmeirim et al. 2013), which is likely augmenting the mass of the filaments. Protostars are surveyed and identified in infrared using, for example, the *Spitzer Space Telescope* (Rebull et al. 2010, 2011). L1495, B213, and B218 have at least one Class I or Flat spectrum protostar, whereas B10, B211, and B216 have no protostar or only one Class II or III protostar, which suggests that L1495/B7, B213, and B218 are relatively more evolved than B10, B211, and B216 in terms of star formation (Seo et al. 2015). Having various evolutionary stages in Taurus enables us to trace the evolutionary processes of low-mass star formation.

Smaller structures in the L1495-B218 regions have been identified using gas velocity information obtained from observations of C^{18}O and NH_3 (Hacar et al. 2013; Seo et al. 2015). Thirty-five velocity-coherent filaments were identified across the L1495-B218 regions and contain a mixture of gravitationally stable and unstable filaments, with line density ranging from 3 to $71 M_\odot \text{pc}^{-1}$ (Hacar et al. 2013) (the critical line density is $16 M_\odot \text{pc}^{-1}$ at 10 K; Ostriker 1964). Thirty-nine NH_3 cores within the filaments are identified and studied in NH_3 (Seo et al. 2015, hereafter Paper I) which have good spatial coincidences with bright dust cores. The dense cores show various evolutionary stages, including 35 starless cores and four protostellar cores (Rebull et al. 2010, 2011). The L1495-B218 filaments and dense cores share a similar surrounding environment, making a consistent survey of the physical and chemical properties of CCS and star formation process possible.

We mapped the 3° long L1495-B218 filaments in CCS $J_N = 2_1-1_0$ and HC_7N $J = 21-20$ using the Robert C. Byrd GBT. We analyze the kinematics of CCS-bright regions and discuss what CCS emission tells us about dense core evolution and star formation. We also analyze the cyanopolyne HC_7N emission that was in the bandpass of previously published NH_3 observations in Seo et al. (2015). Converging-motion tracers, HCN and HCO^+ $J = 1-0$, were observed toward 26 dense cores, including three dense cores with strong CCS emission, using the 12 m radio telescope of the Arizona Radio Observatory (ARO) and the Robert C. Byrd GBT. The layout of this article is as follows: Section 2 briefly introduces our mapping of the L1495-B218 filaments in CCS and the data reduction procedures. In Section 3 we present the basic physical properties of the L1495-B218 filaments seen in CCS and kinematics of three CCS-bright regions. In Section 4 we discuss what CCS traces in a molecular cloud and the physical states of CCS-bright regions by analyzing CCS with ^{12}CO , ^{13}CO , C^{18}O , NH_3 , HCN, and HCO^+ . Finally, we summarize our results in Section 5.

2. Observation and Data Reduction

2.1. Mapping in CCS $J_N = 2_1-1_0$ and HC_7N $J = 21-20$

We observed the L1495-B218 filaments using the GBT in CCS $J_N = 2_1-1_0$ (GBT12A-295 & GBT13A-126) in spring of 2012 and 2013. In the first year, we mapped the filaments in NH_3 (1,1) and (2,2) and HC_7N $J = 21-20$ using seven beams of the K -band focal plane array (KFPA) and in CCS $J_N = 2_1-1_0$ (22.344033 GHz; Yamamoto et al. 1990) using one beam of the KFPA (7+1 mode) from 2012 April to 2013 February (see Paper I). In the second year of observations, we mapped the L1495-B218 filaments in CCS 2_1-1_0 using seven beams. We mapped each region using position switching. Three “off” positions were selected with extinction small enough not to have CCS 2_1-1_0 emission. Pointing of the telescope was updated by observing the quasar 0403+2600 every two hours. To calibrate the gain of seven KFPA beams, we observed either Venus or Jupiter in every observing shift and used the same calibration procedure described in Seo et al. (2015) (hereafter Paper I) to place spectra on the T_{mb} scale. We also observed the peak dust continuum position of the L1489PPC starless core ($\alpha = 04:04:47.6$, $\delta = +26:19:17.9$, J2000.0; Young et al. 2004; Ford & Shirley 2011) in every observing shift for a secondary check on the consistency of the

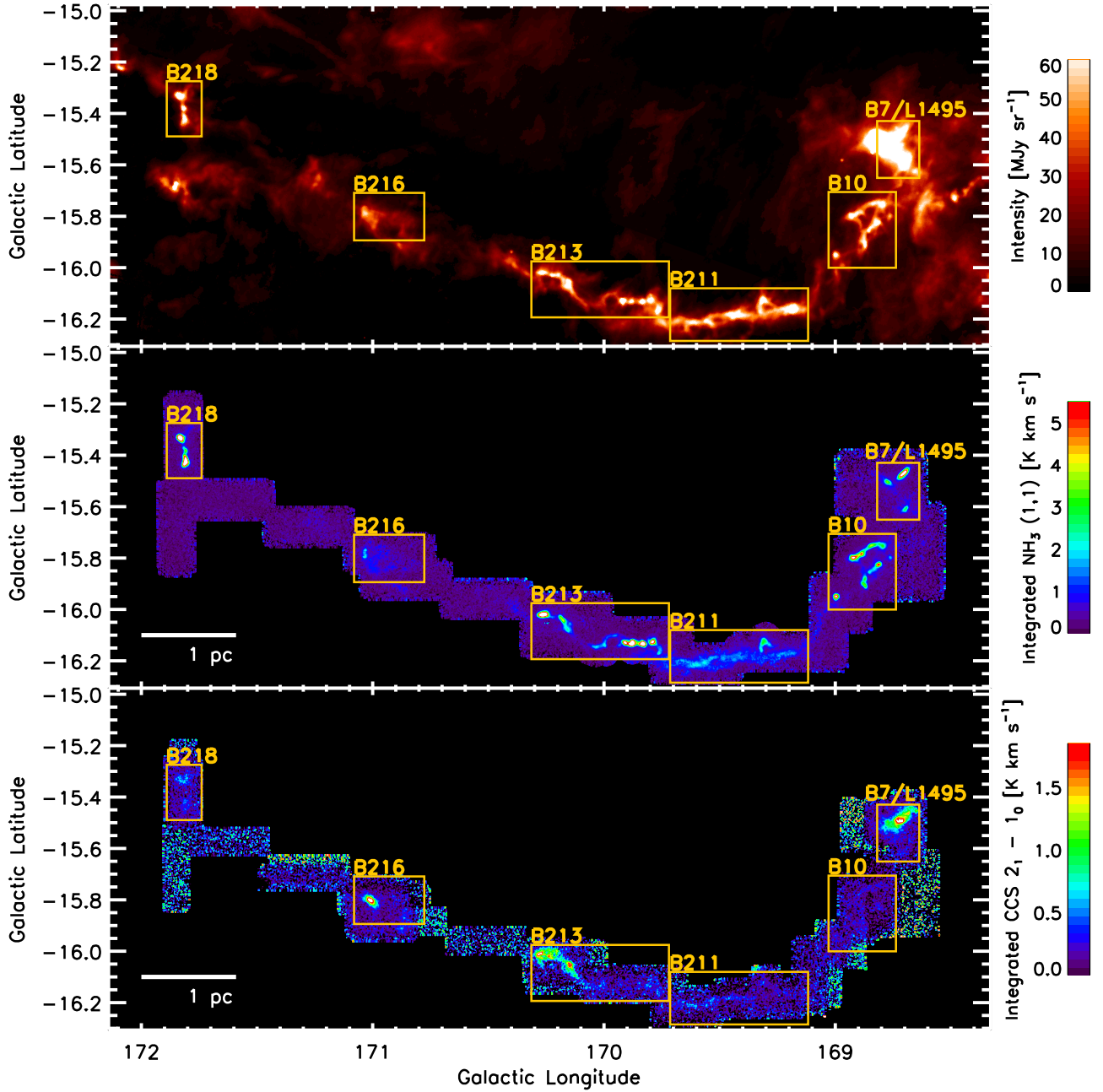


Figure 1. Top: 500 μm dust continuum emission seen by the SPIRE instrument on the *Herschel Space Observatory* (Palmeirim et al. 2013). Middle: map of integrated intensity of NH_3 (1,1) (Seo et al. 2015). Bottom: map of integrated intensity of CCS $J_N = 2_1-1_0$.

absolute flux calibration. The FWHM beam size of the GBT at 22 GHz is $31''$.

The CCS data have been reduced in the same way as described in Paper I. Figure 1 shows the integrated intensity map of CCS $J_N = 2_1-1_0$, and Figure 2 shows the rms of the CCS map. We deeply mapped the regions with the NH_3 (1,1) emission above 300 mK and the region with the 500 μm continuum emission above 20 MJy sr^{-1} . We used all seven beams of the KPFA and achieved an rms noise of ≤ 200 mK. The median noise level is 154 mK with the lowest noise level of 26 mK in L1495.

The HC_7N data have been reduced in the same way as described in Paper I. The rms of the HC_7N map is the same as the rms map of NH_3 shown in Paper I because $\text{HC}_7\text{N } J = 2_1-2_0$ is in the same bandpass as NH_3 (1,1) and (2,2).

2.2. HCN and HCO^+ 1–0 Observations

We observed the 89 GHz transitions of HCN and HCO^+ to probe the internal dynamics of dense cores. We surveyed 26 dense cores, including L1495A-N, L1521B, and L1521D in $\text{HCN } J = 1-0$ (88.631847 GHz) and $\text{HCO}^+ J = 1-0$ (89.1885 GHz), in the winters of 2013, 2016, and 2017. We used the 12 m ARO and the Argus receiver on the 100 m GBT (Devaraj et al. 2015) (GBT16B-114). Coordinates of L1495A-N, L1521B, and L1521D are $(\alpha, \delta) = 4:18:33.0, +28:27:58$, $(\alpha, \delta) = 4:24:20.6, +26:36:02$, and $(\alpha, \delta) = 4:21:21.7, +26:59:31$, respectively, in J2000.0. The details of the HCN and HCO^+ survey will be reported in a separate article.

The ARO has a single beam with FWHM beam size of $66''$ at 89 GHz. For an accurate calibration of the 12 m ARO data, we

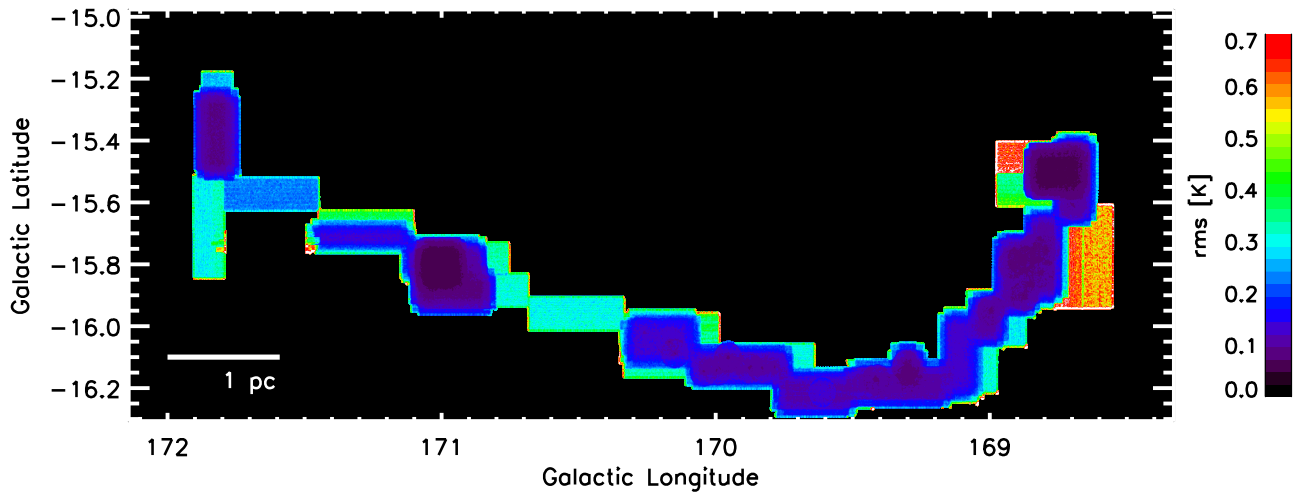


Figure 2. rms of the CCS map in T_{mb} at a spectral resolution of 6.1 kHz (corresponding to 0.082 km s^{-1}), obtained by smoothing two spectral channels.

observed Jupiter every 1.5 hr to adjust focus and pointing and to calibrate the spectra onto the T_{mb} scale. The system temperatures were around 180 K in T_A . The main beam efficiency was typically $\simeq 0.6$. A linear baseline was removed by the position switching. The total integration time for each target was 30 minutes, with a typical rms of $<120 \text{ mK}$ in units of T_{mb} unit at a spectral resolution of 0.041 km s^{-1} . We reduced the data using the CLASS software (Pety 2005).

Argus is a 16-pixel W -band array receiver with a 4×4 configuration on the GBT (Sieth et al. 2014). We used Beam 10 as the pointing beam on the three cores and the other beams to sparsely map the outskirts of the cores. The FWHM beam size is $9''$ at 88 GHz. For calibration, we observed the blazar J0510+1800, which is an Atacama Large Millimeter/submillimeter Array calibration source, to obtain the focus and pointing solutions and to calibrate the spectra in units of main beam temperature. The system temperatures were $\simeq 150 \text{ K}$ in T_A^* . The main beam efficiencies were typically 0.4 for all beams. A continuum baseline was removed by the frequency switching observation with a total shift of 7 kHz ($\pm 3.5 \text{ kHz}$ shift). The total integration time for each target was 10 minutes, resulting in an rms generally less than 150 mK in T_{MB} at a spectral resolution of 0.041 km s^{-1} . We reduced the data using the GBTIDL package (Marganian et al. 2006) provided by the Green Bank Observatory.

3. Results

3.1. Integrated Intensities of CCS $J_N = 2_1-1_0$ and $\text{HC}_7\text{N } J = 21-20$

We present the integrated intensity of CCS $J_N = 2_1-1_0$ emission (hereafter CCS 2_1-1_0) in Figures 1 and 3. The CCS 2_1-1_0 emission is bright ($>1 \text{ K km s}^{-1}$) mainly in three regions: north of L1495/B7 (L1495A/B7N), east of B213 (hereafter B213E), and B216. There is also weak emission in B211 and B218. No significant CCS 2_1-1_0 emission is observed in B10 and west of B213 (hereafter B213W) at our noise level (we detect only a hint of the emission at the 2σ level). The lowest intensity of $500 \mu\text{m}$ dust continuum emission where the CCS 2_1-1_0 intensity is above 3σ (210 mK) is 15 MJy sr^{-1} , whereas it is 25 MJy sr^{-1} for NH_3 (1,1); however, not all structures at 15 MJy sr^{-1} have CCS 2_1-1_0 emission. In B10, we do not have a solid detection of CCS 2_1-1_0 emission at our rms level of 70 mK , even though the

dust continuum intensity spans the range from $<15 \text{ MJy sr}^{-1}$ to 250 MJy sr^{-1} . This confirms that CCS 2_1-1_0 emission traces lower density structures compared to NH_3 (1,1) but not every low-density structure. For example, CCS 2_1-1_0 emission is bright in both more-evolved (L1495A/B7N and B213E) and less-evolved (B216) regions, whereas it is weak or not detected in a couple of less-evolved regions (B10 and B211) (see Seo et al. 2015, for an explanation of the evolutionary stages of regions).

We compare our CCS 2_1-1_0 map to an NH_3 (1,1) map (Seo et al. 2015) and a dust continuum map at $500 \mu\text{m}$ (Palmeirim et al. 2013) in Figure 3. In general, the peak intensities of CCS 2_1-1_0 emission are displaced from the intensity peaks of NH_3 and dust continuum, whereas the intensity peaks of the NH_3 and the $500 \mu\text{m}$ dust continuum are spatially well correlated.

The peak intensities of CCS 2_1-1_0 emission in L1521D and L1495A-N are at the outskirts of the NH_3 cores, $\sim 0.1 \text{ pc}$ from the NH_3 (1,1) intensity peaks (2.5 at the distance to Taurus, 140 pc ; Loinard et al. 2007; Torres et al. 2009), and show an arc-shaped morphology that partially surrounds the NH_3 cores. CCS 2_1-1_0 emission is also bright at a clump located at 0.35 pc southwest of L1521D. The clump contains NH_3 dense cores No.30, No.31, and No.32 (see Figure 9 in Paper I). Among the three cores, CCS 2_1-1_0 emission is brightest at the NH_3 core No.32, and the position of intensity peak agrees relatively well (within 0.05 pc or $74''$, which is a rare occurrence in this mapping survey) with the dust and NH_3 peaks. In B216, which is thought to be a less-evolved region, the CCS 2_1-1_0 peak is located about 0.1 pc west of the NH_3 (1,1) and dust continuum intensity peaks. Notably, the CCS 2_1-1_0 intensity peaks are spatially displaced from the NH_3 cores identified in Paper I. This suggests that CCS 2_1-1_0 emission does not trace the dense core in this region.

We compare $\text{HC}_7\text{N } J = 21-20$ (hereafter $\text{HC}_7\text{N } 21-20$) emission to CCS 2_1-1_0 and NH_3 (1,1) emission in Figure 4. $\text{HC}_7\text{N } 21-20$ emission is only detected in L1495A-N and L1521D at our rms level of $\sim 85 \text{ mK}$. $\text{HC}_7\text{N } 21-20$ emission has a good correlation with strong CCS 2_1-1_0 emission of $>1 \text{ K}$ in both L1495A-N and L1521D. Similar to the CCS 2_1-1_0 emission, the $\text{HC}_7\text{N } 21-20$ intensity peaks do not agree with the NH_3 (1,1) intensity peaks or the dust continuum intensity peaks. Also, the $\text{HC}_7\text{N } 21-20$ emission in B213E has an arclike shape that surrounds an NH_3 dense core. On the other hand, $\text{HC}_7\text{N } 21-20$ emission is not as spatially extended

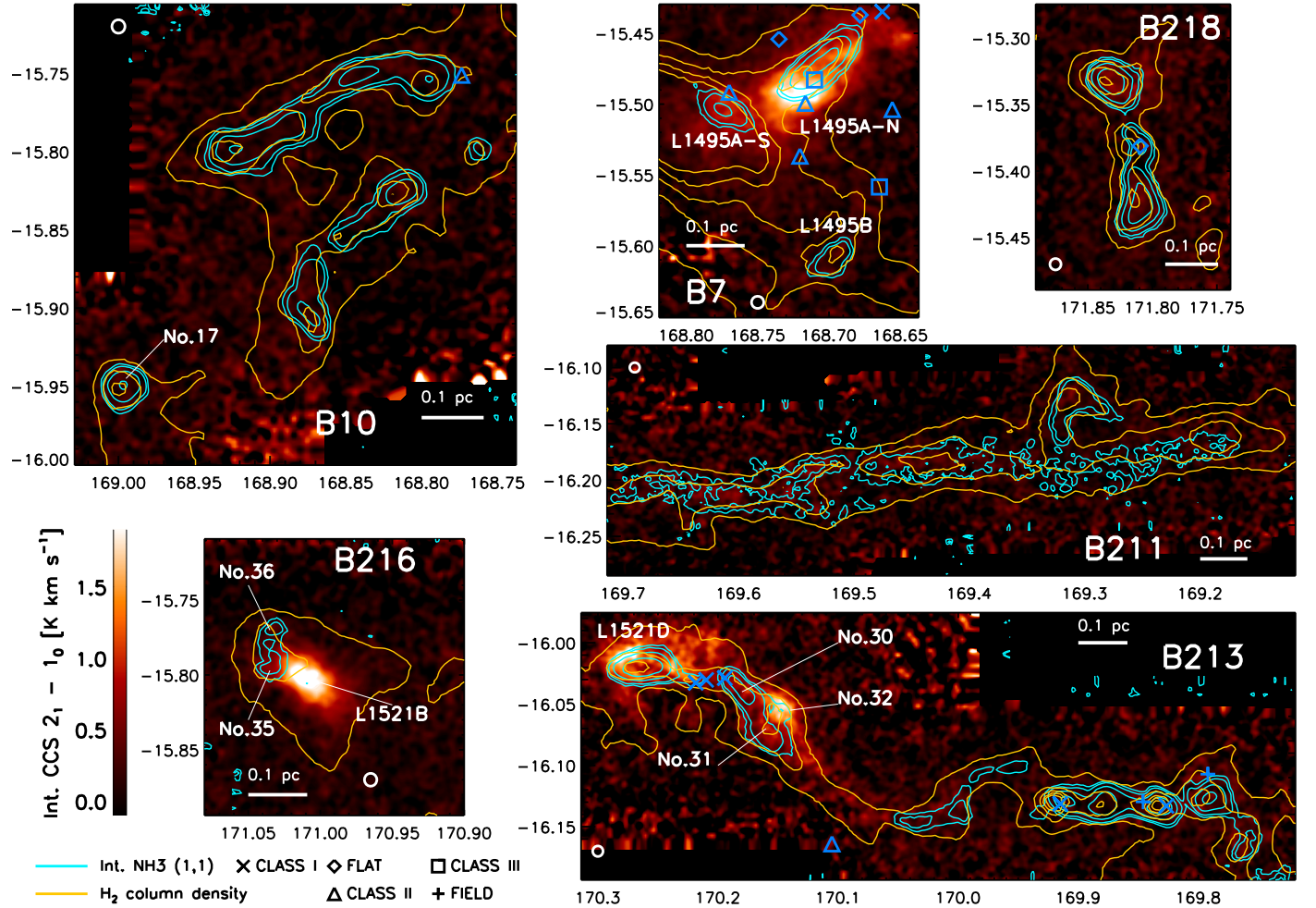


Figure 3. Images of integrated CCS 2_1-1_0 (color), integrated NH₃ (1,1) (cyan contours), H₂ column density (orange contours), and positions of known protostars. The X-axis is Galactic longitude, and the Y-axis is Galactic latitude. NH₃ contours are at integrated intensities of 1, 1.5, 3, 6, and 12 K km s⁻¹. H₂ column-density contours are at 5×10^{21} , 1×10^{22} , 1.5×10^{22} , 2×10^{22} , and 2.5×10^{22} cm⁻². The names of previously studied cores discussed in this study are indicated in the images. For the dense cores discussed in this study but not having classical names, we used the identification numbers of NH₃ cores in Seo et al. (2015). The white circle in each image shows the beam size.

as CCS 2_1-1_0 emission, and the peak intensity of HC₇N 21–20 emission is less than 0.7 K in all regions, which is much weaker than CCS 2_1-1_0 intensity peaks (>2 K). The intensity peaks of HC₇N 21–20 emission are also slightly displaced from the CCS 2_1-1_0 intensity peaks. This may be due to different excitation conditions ($E_u^{\text{CCS}}/k = 1.61$ K whereas $E_u^{\text{HC}_7\text{N}}/k = 12.5$ K) and different chemical processes of CCS 2_1-1_0 and HC₇N 21–20, even though they are both carbon-chain molecules (see further discussion in Section 4).

3.2. Spectral Line Fitting

Most of CCS 2_1-1_0 spectra in our survey are well described by a single Gaussian profile, but some of CCS 2_1-1_0 spectra show skewed and double-peak profiles. Therefore, to understand the physical properties of observed CCS 2_1-1_0 structures in the L1495-B218 filaments, we fit CCS 2_1-1_0 lines with three different spectra models: single Gaussian, skewed Gaussian, and double Gaussian profiles. We use a least χ^2 fit to the observed profile assuming the following model profiles:

$$\phi_{\text{single}}(v) = A \exp\left(-\frac{(v - v_{\text{lsr}})^2}{2\sigma^2}\right) \quad (1)$$

$$\phi_{\text{skewed}}(v) = A \exp\left(-\frac{(v - v_{\text{lsr}})^2}{2\sigma^2}\right) \left[1 + \text{erf}\left(\frac{\alpha(v - v_{\text{lsr}})}{\sqrt{2}\sigma}\right)\right] \quad (2)$$

$$\phi_{\text{double}}(v) = A_1 \exp\left(-\frac{(v - v_{\text{lsr},1})^2}{2\sigma_1^2}\right) + A_2 \exp\left(-\frac{(v - v_{\text{lsr},2})^2}{2\sigma_2^2}\right) \quad (3)$$

where v is the velocity, v_{lsr} is the LSR velocity of the line, σ is the velocity dispersion, A is the peak line intensity, α is the skewness, and the subscripts 1 and 2 denote velocity components in the double Gaussian model. We found that the χ^2 values are typically lower with fits using the skewed Gaussian model relative to the single Gaussian, because the skewed Gaussian model has one more degree of freedom in the line fitting. We used the single Gaussian model rather than the skewed Gaussian model if χ^2 values from both models are less than 3σ .

Figure 5 shows examples of observed CCS 2_1-1_0 lines and best-fit models. CCS 2_1-1_0 lines in all regions are fitted with single Gaussian profiles except in small portions of L1495A

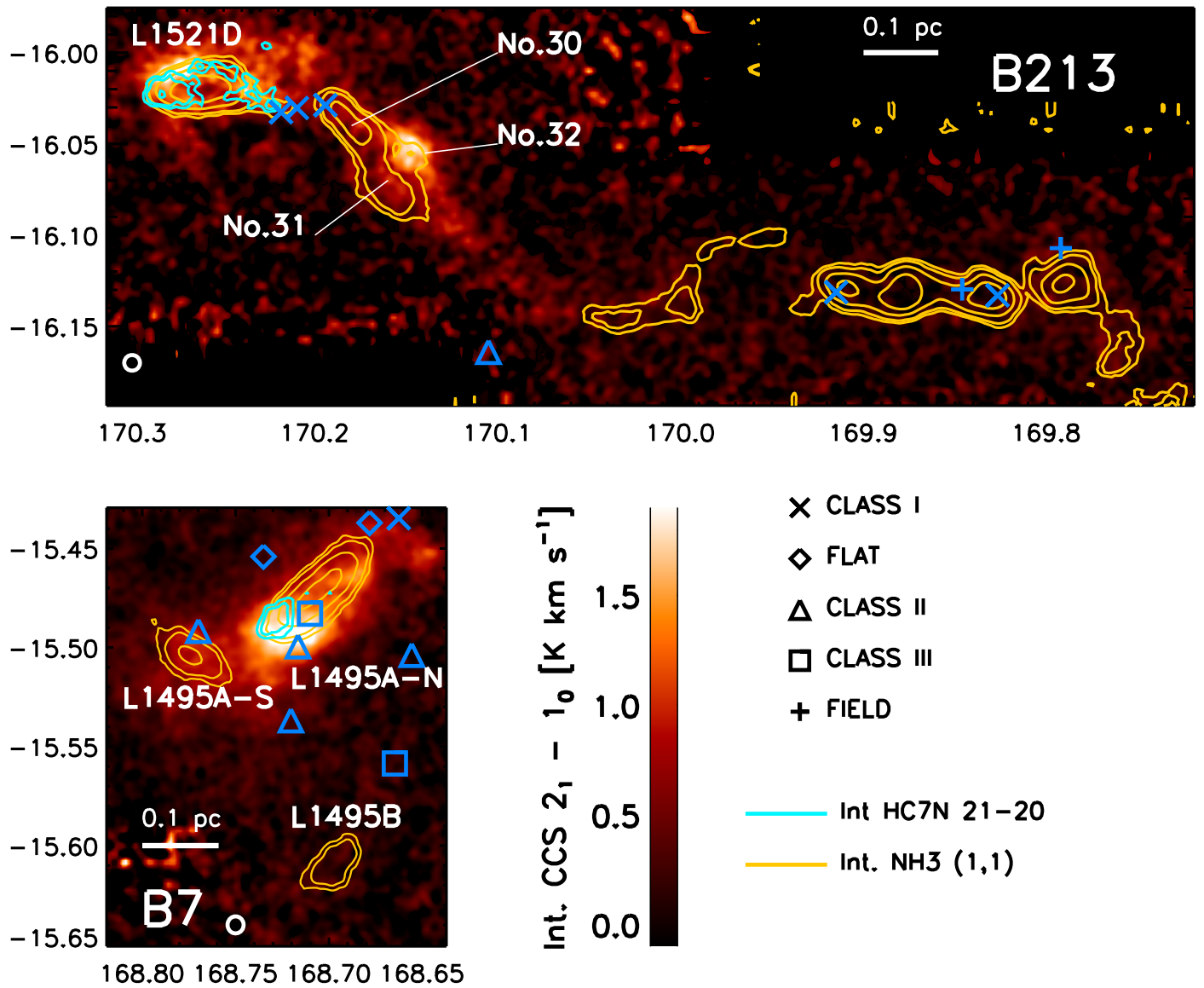


Figure 4. Images of integrated CCS 2_1-1_0 (color), integrated NH₃ (1,1) (orange contours), HC₇N 21–20 (cyan contours), and positions of known protostars. The X-axis is Galactic longitude, and the Y-axis is Galactic latitude. NH₃ contours are at integrated intensities of 1, 1.5, 3, 6, and 12 K km s^{−1}. HC₇N contours are at integrated intensities of 0.1, 0.15, 0.3, 0.6, and 1.2 K km s^{−1}. The names of previously studied cores discussed in this study are indicated in the images. For the dense cores discussed in this study but not having classical names, we used the identities of NH₃ cores in Seo et al. (2015). The white circle in each image shows the beam size.

and B213E and the central part of B216. The number of spectra fitted with skewed Gaussian profiles is less than 5% of the total number of spectra in every region. In B216, we found that there are two intensity peaks at 6.25 km s^{−1}, and 6.5 km s^{−1} and the CCS 2_1-1_0 lines in the region are the better fit with double Gaussian profiles as indicated by reduced values of χ^2 .

Figure 6 shows distributions of the LSR velocity of CCS 2_1-1_0 and NH₃ (1,1) emission in L1495A/B7N, B213E, and B216. In L1495A/B7N, the peaks of the LSR velocity distribution of CCS 2_1-1_0 emission and NH₃ emission show a good agreement with each other, which indicates that NH₃ (1,1) emission and CCS emission trace the same dense structures in this region. On the other hand, the LSR velocity range of CCS emission is considerably wider than that of NH₃ (1,1) emission with a long tail toward redshifted velocity, which suggests that CCS 2_1-1_0 emission traces extended structures in this area. In B216, the CCS 2_1-1_0 and NH₃ (1,1)

emission overlap each other in the LSR velocity range from 6.2 to 6.6 km s^{−1} but NH₃ (1,1) is more extended to 6.8 km s^{−1}. The histogram of the LSR velocity of CCS 2_1-1_0 emission shows two peaks at 6.25 and 6.5 km s^{−1}, whereas that of NH₃ emission shows a single peak at 6.6 km s^{−1}. Having CCS 2_1-1_0 emission at two velocities and a displacement between CCS 2_1-1_0 and NH₃ (1,1) intensity peaks suggests that B216 may be either a complex region with multiple dense structures at different LSR velocities or there may be a converging flow. However, we did not see any blue asymmetry in the HCN or HCO⁺ 1–0 line profile, indicating that there is no significant converging motion. B213E includes four dense cores, and their LSR velocity ranges from 6.3 to 7.2 km s^{−1}. There are three peaks in the distribution of LSR velocity, and two of them coincide with NH₃ LSR velocity peaks. The peak at 6.9 km s^{−1} is related of NH₃ core No.32 in the west of B213E. The other two peaks at 6.4 and 6.6 km s^{−1} are related to L1521D. The

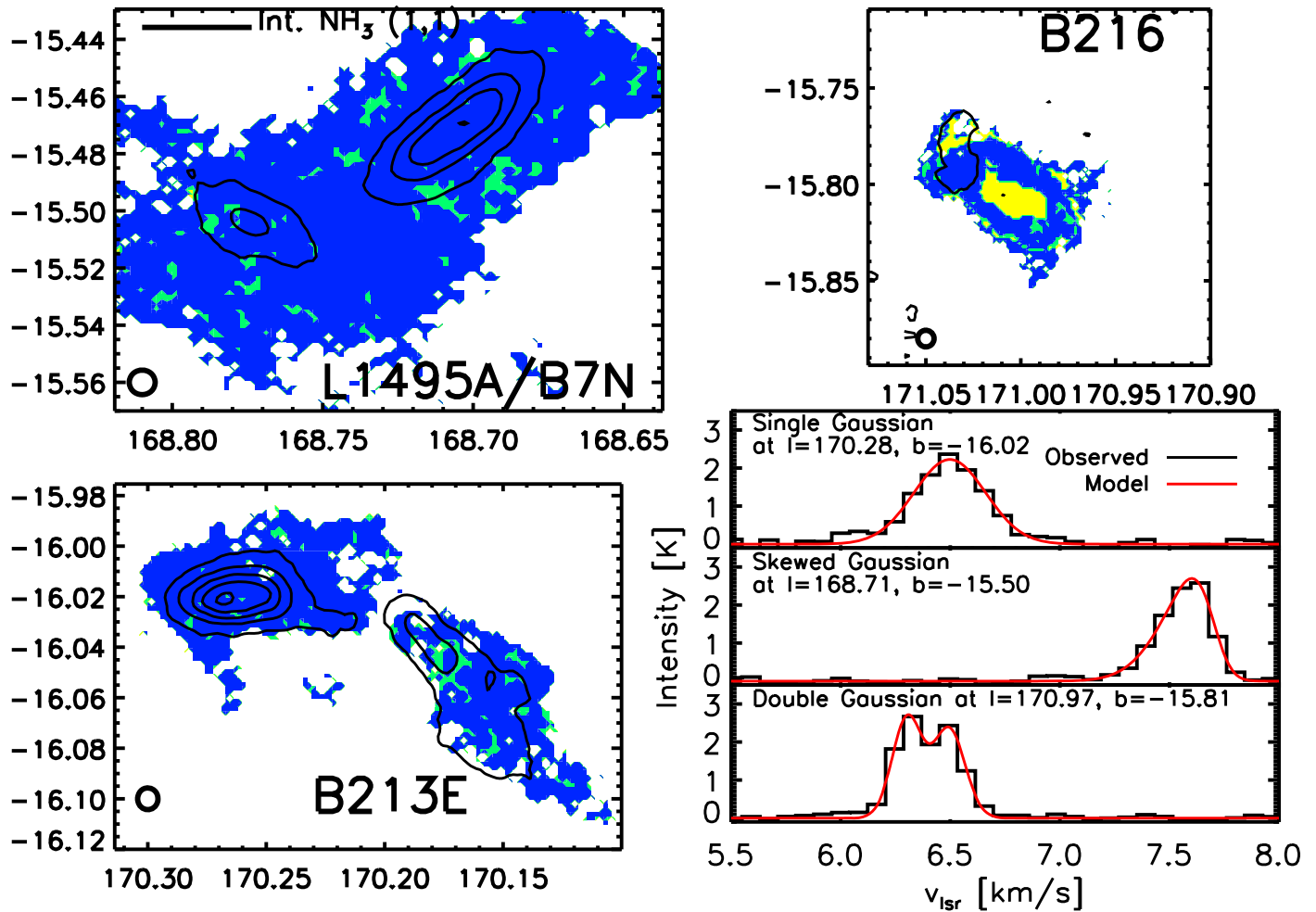


Figure 5. Left and upper right panels: images of spectral fitting models (color) for CCS 2_1-1_0 lines with the integrated intensity of NH_3 (1,1) (black contours). Blue, cyan, and yellow denote areas in which single, skewed, and double Gaussian models, respectively, are used to fit spectral lines. NH_3 contours are at integrated intensities of 1, 1.5, 3, 6, and 12 K km s^{-1} . The black circle in each panel shows beam size. Single Gaussian fitting is forced unless χ^2 is greater than 9 in the single Gaussian fitting. Left right panel: examples of spectra model fitting (red lines) to the observed lines (black lines). The top panel shows an example of single Gaussian fitting, the middle panel shows an example of skewed Gaussian fitting, and the bottom panel shows an example of double Gaussian fitting. The Galactic coordinates of the example spectra are written in each panel.

LSR velocity ranges observed in CCS 2_1-1_0 and NH_3 (1,1) are quite similar.

Using the fitted profiles of CCS 2_1-1_0 lines, we estimated the column density of CCS under assumption of the optically thin emission. The CCS 2_1-1_0 emission in dense cores is generally optically thin (Wolkovitch et al. 1997; Rosolowsky et al. 2008). The estimated column density of CCS ranges from 1×10^{12} to $3 \times 10^{13} \text{ cm}^{-2}$ when we assume the excitation temperature is the same as the kinetic temperature. The median column density is $7 \times 10^{12} \text{ cm}^{-2}$. If we assume that the excitation temperature is 6 K, which is the excitation temperature found in TMC1, the column density is in the range of 1×10^{12} – $4 \times 10^{13} \text{ cm}^{-2}$. This column-density range is similar to the CCS column densities found in other dense cores and Bok globules (e.g., Suzuki et al. 1992; Wolkovitch et al. 1997; Marka et al. 2012). Using a Monte-Carlo radiative transfer calculator, we found that the optical depth of CCS 2_1-1_0 for this column-density range is <0.5 with the median optical depth of 0.1, which is consistent with the optically thin assumption.

We also fitted HC_7N 2_1-2_0 and evaluated the column density of HC_7N under the optically thin limit. The profiles are

well fitted with single Gaussian profiles and the column-density ranges $(1-5) \times 10^{11} \text{ cm}^{-2}$ when we assume that the excitation temperature is same as the ammonia kinetic temperature ~ 10 K. The HC_7N column density is roughly a factor of two larger if the excitation temperature is 4 K.

3.3. Kinematics

3.3.1. L1495A-N

We probe the kinematics of dense core L1495A-N using spectral maps of CCS 2_1-1_0 and NH_3 (1,1) and investigate the motions of filaments and dense cores traced by the CCS 2_1-1_0 emission. Figure 7 presents channel maps of the CCS 2_1-1_0 emission along with the integrated intensity of NH_3 (1,1) in the B7 region. The LSR velocities of NH_3 dense cores are 7.2 and 7.25 km s^{-1} at their centers. The first panel in Figure 7 shows the blueshifted CCS emission relative to the NH_3 (1,1) emission in L1495A-N, whereas the two right panels present the redshifted CCS 2_1-1_0 emission relative to the NH_3 (1,1) emission in L1495A-N. In the first panel, the blueshifted CCS 2_1-1_0 emission is bright in the northeastern part of L1495A-N and elongated similar to the NH_3 core. With increasing LSR

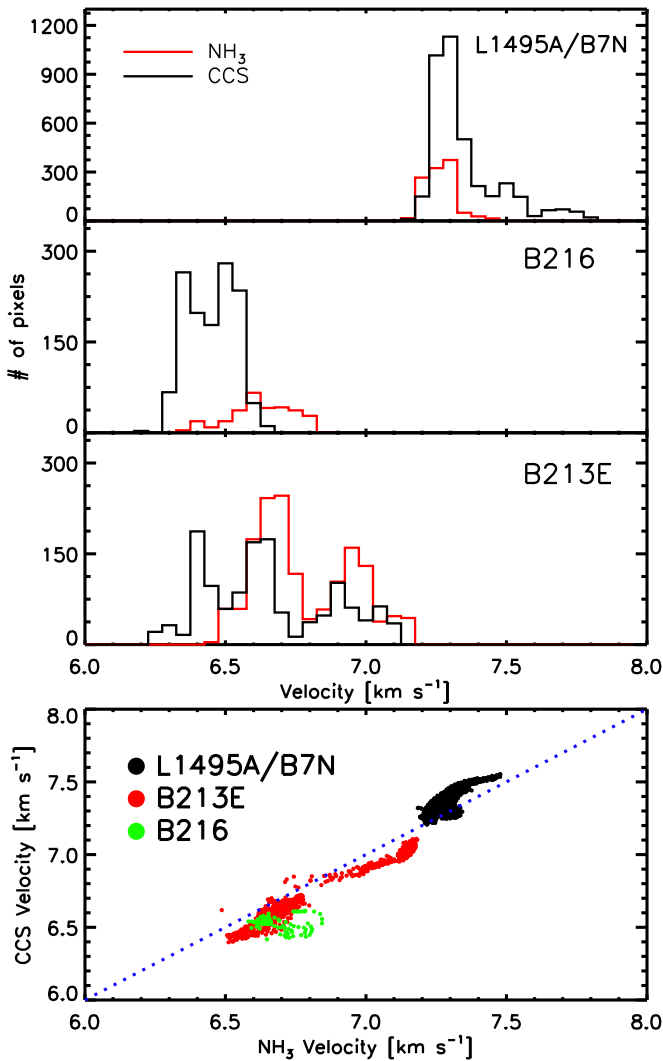


Figure 6. Top: histograms of the LSR velocities in L1495A/B7N, B213E, and B216. Bottom: CCS 2_1-1_0 velocity vs. NH₃ velocity. Red histograms denote the LSR velocities of NH₃ emission, and black histograms denote the LSR velocities of CCS 2_1-1_0 emission in the top panel. In the bottom panel, each point corresponds to a pixel that has both CCS and NH₃ emission.

velocity, we find that CCS 2_1-1_0 emission moves toward the southeast direction, which indicates that L1495A-N has shear flows, or rotation, or converging flows.

We investigate the flow of gas using the LSR velocity maps of CCS 2_1-1_0 and NH₃ (1,1) (Figure 8). We find a steep transition in the LSR velocities of both CCS 2_1-1_0 and NH₃ (1,1) emission within L1495A-N (pointed with black arrow). The transition shows a velocity shift of 0.3 km s^{-1} within the size of beam (0.022 pc) and the steepest velocity gradient of $\sim 14 \text{ km s}^{-1} \text{ pc}^{-1}$ in both NH₃ (1,1) and CCS 2_1-1_0 , which is at least seven times larger than the typical velocity gradient measured for rotation ($\sim 2 \text{ km s}^{-1} \text{ pc}^{-1}$, Goodman et al. 1993). Also, the transition is parallel to the long axis of L1495A-N rather than its short axis, which is a rare case. Only L183 is reported to have the rotation axis parallel to its long axis (Kirk et al. 2009). However, the velocity gradient of L1495A-N is considerably larger than that of L183 ($8.9 \text{ km s}^{-1} \text{ pc}^{-1}$). Thus, an unusually large gradient of the LSR velocity in L1495A-N may be due to a converging flow or a shear flow, but not all of it is due to rotation.

To check whether the flow in L1495A-N is a converging flow, we observed L1495A-N in HCN $J=1-0$ and HCO⁺ $J=1-0$ using the 12 m ARO and 100 m GBT. The beam of the 12 m ARO covers most of L1495A-N; thus, the HCN $1-0$ and HCO⁺ $1-0$ observations using the 12 m ARO show the overall internal dynamics of L1495A-N. We found that L1495A-N has strong blue asymmetric profiles in both HCO⁺ and HCN $J=1-0$ (Figures 9 and 10), whereas optically thin CCS 2_1-1_0 and NH₃ (1,1) lines are well-fitted by a single Gaussian profile. To see whether the blue asymmetric profiles are due to self-absorption of a converging motion, we estimated the optical depths of HCN and HCO⁺ $1-0$ lines through our chemical model followed by LTE-radiative-transfer model (Majumdar et al. 2017a) and found their optical depths to be larger than 2 in L1495A-N. Also, ¹³CO $1-0$ has two peaks at 6 and 7.2 km s^{-1} , which do not coincide the two intensity peaks of HCN and HCO⁺ $1-0$. These results indicate that the blue asymmetric profiles of HCN and HCO⁺ $1-0$ are not due to two different velocity components along the line of sight but are the results of self-absorption, which is often observed in collapsing dense cores (e.g., Lee et al. 1999; Sohn et al. 2007).

All hyperfine components of HCN $J=1-0$ observed using the ARO show blue asymmetric line profiles. The converging-flow velocities estimated using a simple two-layer model (Equation (9) in Myers et al. 1996) are 0.41 km s^{-1} for $F=2-1$, 0.17 km s^{-1} for $F=1-1$, and 0.10 km s^{-1} for $F=0-1$. The converging-flow speed measured in HCO⁺ $1-0$ is 0.83 km s^{-1} , which is roughly four times larger than the sound speed. This converging-flow speed is higher than the maximum infall speed in a similarity solution of a gravitationally collapsing core (Larson 1969; Penston 1969) and is similar to that formed in the collapse of dense core triggered by a supersonic converging flow (Gong & Ostriker 2009).

Sparsely mapped HCN and HCO⁺ using Argus on the GBT shows the dynamics of L1495A-N at higher angular resolution (Figure 10). Although the 12 m ARO data show overall dynamics of L1495A-N, the GBT data show spatially resolved dynamics within L1495A-N and its surroundings because the beam size of GBT is much smaller than that of L1495A-N. Dense cores mapped previously in HCN $1-0$ and HCO⁺ $1-0$, such as L1544, L694-2, and L1197, all have strongest emission and largest infall speed (converging-flow speed due to gravitational collapse) at or near the core center and show a roughly azimuthally symmetric distribution of emission. On the contrary, L1495A-N has highly asymmetric distributions of HCN and HCO⁺ intensities and converging-flow speeds. The brightest emission from HCN and HCO⁺ is found on the northeast outskirts of the core rather than its center. Moreover, the converging-flow speeds are also the largest at northeast outskirts (0.9 km s^{-1} or Mach 4.5), whereas the west side of L1495A-N shows almost no converging flow ($<0.05 \text{ km s}^{-1}$). The quasi-static collapse models of a gas sphere and filaments typically have the maximum infall velocity less than Mach 4, and the fastest infall occurs very close to the core center or the axis of the filament ($<0.01 \text{ pc}$) at the final stage of the collapse (Foster & Chevalier 1993; Myers 2005; Gong & Ostriker 2009; Seo et al. 2013; Burge et al. 2016). The high converging-flow speed only at the outskirts and the large degree of asymmetry seen in L1495A-N do not agree with the quasi-static collapse models and suggest that large-scale gas flows are likely driving the dynamics of L1495A-N.

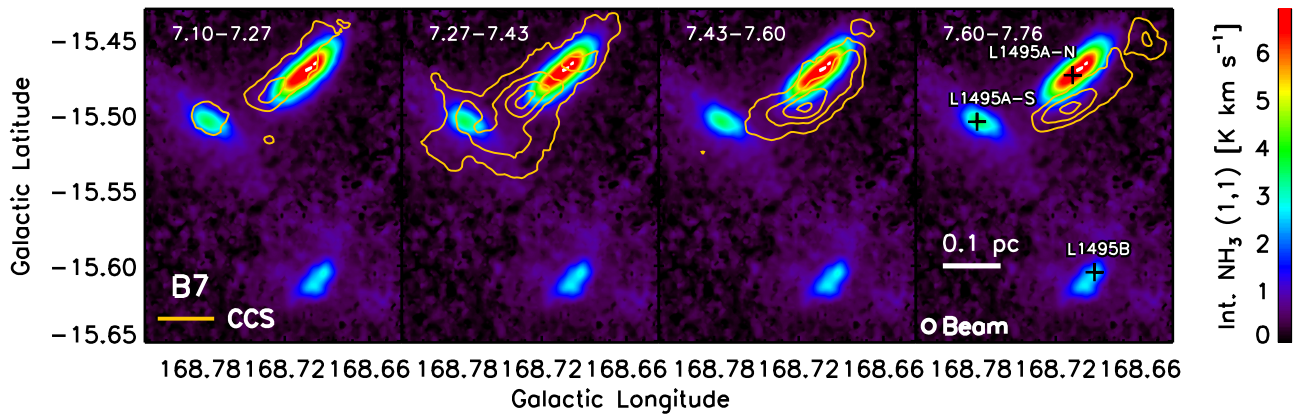


Figure 7. Channel map of CCS 2_1-1_0 (contours) and integrated intensity of NH_3 (1,1) (color) in L1495/B7. CCS 2_1-1_0 contours start at 0.1 K km s^{-1} and increase in steps of 0.1 K km s^{-1} . The velocity range for each channel map is given at the top of each panel in units of km s^{-1} . Names of the dense cores are written in the last panel.

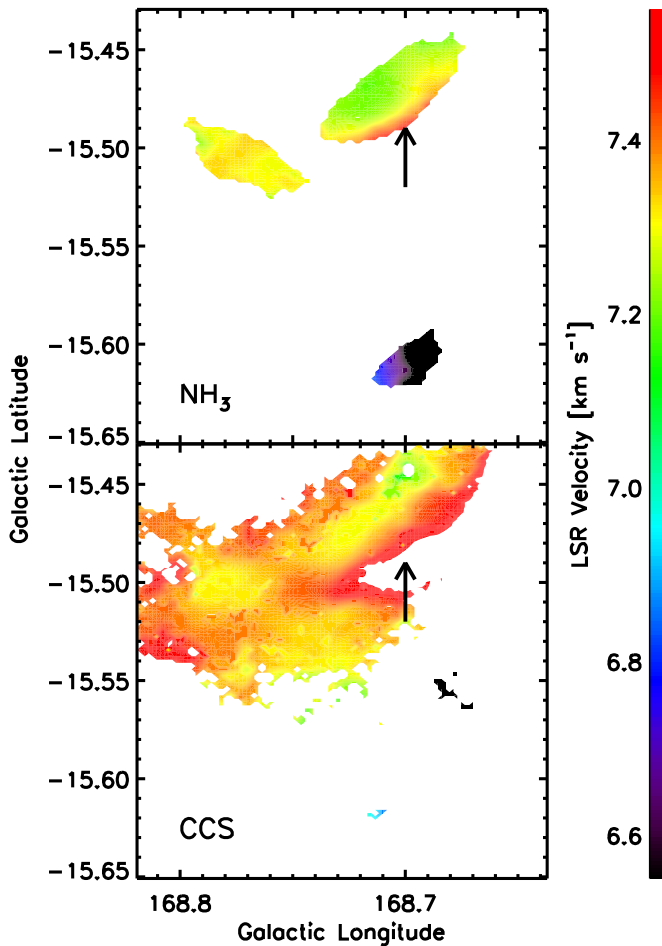


Figure 8. Maps of NH_3 (1,1) (top) and CCS 2_1-1_0 (bottom) LSR velocities in L1495. The black arrow points to the steep transition in the LSR velocity within L1495A-N.

To see whether the converging flow observed in L1495A-N in HCN $1-0$ and $\text{HCO}^+ 1-0$ is connected with a large-scale flow, we examine $^{13}\text{CO } 1-0$ integrated intensity and channel maps along with the integrated intensity map of NH_3 (1,1) in Figure 11. The $^{13}\text{CO } 1-0$ is observed using the 14 m FCRAO with a spatial resolution of $47''$ and a velocity resolution of

0.256 km s^{-1} (Goldsmith et al. 2008). We found that there are roughly three different groups of ^{13}CO structures radiating from L1495 in the integrated intensity map and found in the channel maps that the hub region may be a place where the three groups of ^{13}CO structures are colliding or converging (upper panel of Figure 11). In Figure 11, we show the three groups of CO structures with the velocity ranges chosen to emphasize each group of ^{13}CO structures. One group of ^{13}CO structures (Group I at $6.28-6.54 \text{ km s}^{-1}$) stretches from the hub to B10, B213, and B216 and forms the L1495-B218 filaments. Another group of ^{13}CO structures (Group II at $6.79-7.05 \text{ km s}^{-1}$) is distributed from the hub and extends to a southwest direction. The last group of ^{13}CO structures (Group III at $7.55-7.81 \text{ km s}^{-1}$) stretches from the hub to the west direction. We also present channel maps in a full velocity range from 6.28 to 7.81 km s^{-1} in Figure 12 to probe the hub and the three groups in the Position–Position–Velocity (PPV) space. The $^{13}\text{CO } 1-0$ emission from 7.05 to 7.55 km s^{-1} is the CO emission from the hub. Group III connects to the hub from redshifted velocity and has the velocity gradient of roughly $-0.8 \text{ km s}^{-1} \text{ pc}^{-1}$ from the Group I to the hub. On the other hand, Groups I and II are at blueshifted velocities and bifurcate from the hub with the velocity gradients of $0.6 \text{ km s}^{-1} \text{ pc}^{-1}$ and $2 \text{ km s}^{-1} \text{ pc}^{-1}$, respectively. The velocity gradients are the median values of the velocity gradients measured following 1 pc distance along the three groups of ^{13}CO structures from L1495A-N (Figure 13). Groups II and III seem to be converging toward the same location in the hub, whereas Group I connects to a position slightly to the south. The fact that the velocity gradients of the three groups are toward the hub with signatures of converging motions in the HCN $1-0$ and $\text{HCO}^+ 1-0$ observations and that the hub is the most massive and gravitational unstable part of the region on the basis of a virial calculation suggest that the velocity gradients of the three groups are likely due to accretion of gas on the hub along the filaments (Seo et al. 2015).

We found that L1495A-N is embedded within the hub in PPV space and exactly located where Groups II and III interface with each other in a zoomed view of L1495A-N with ^{13}CO channel maps (bottom panel of Figure 11). The LSR velocity of $^{13}\text{CO } 1-0$ emission also connects seamlessly with the LSR velocity of NH_3 and CCS emission, and the difference

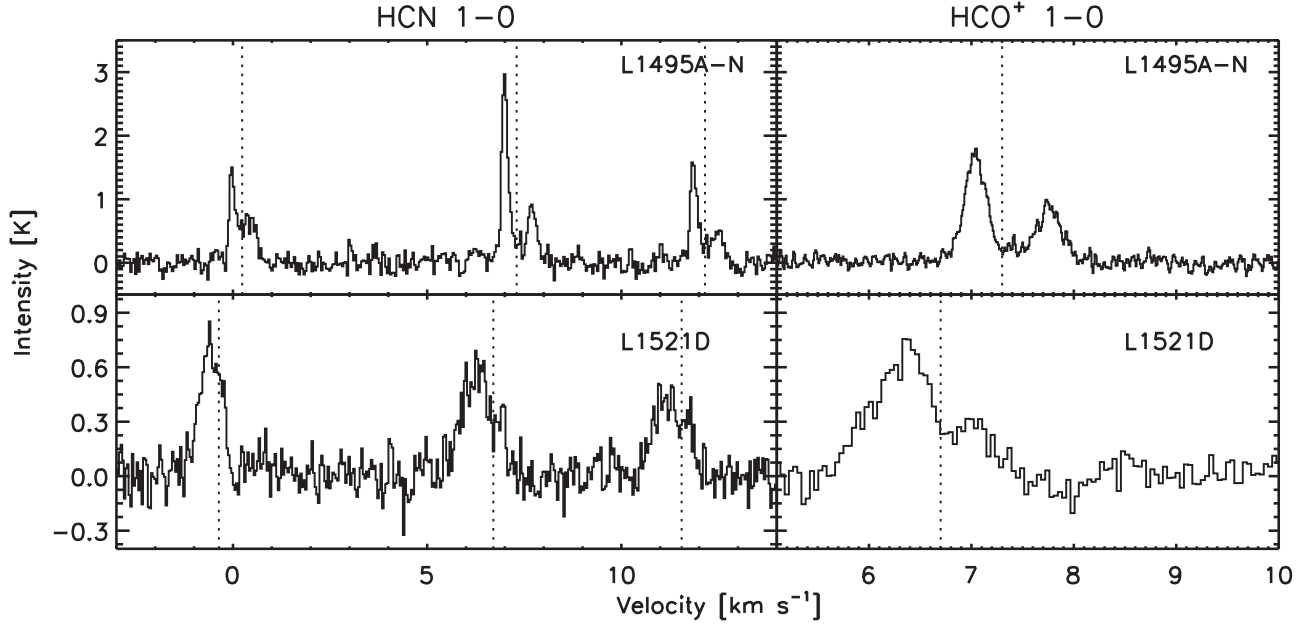


Figure 9. HCN 1–0 (left column) and HCO^+ 1–0 (right column) in L1495A-N (top) and L1521D (bottom). The HCN transition contains three hyperfine components $F = 1-0$ (left), $F = 2-1$ (center), and $F = 1-1$ (right). The dashed vertical lines denote the LSR velocity of NH_3 .

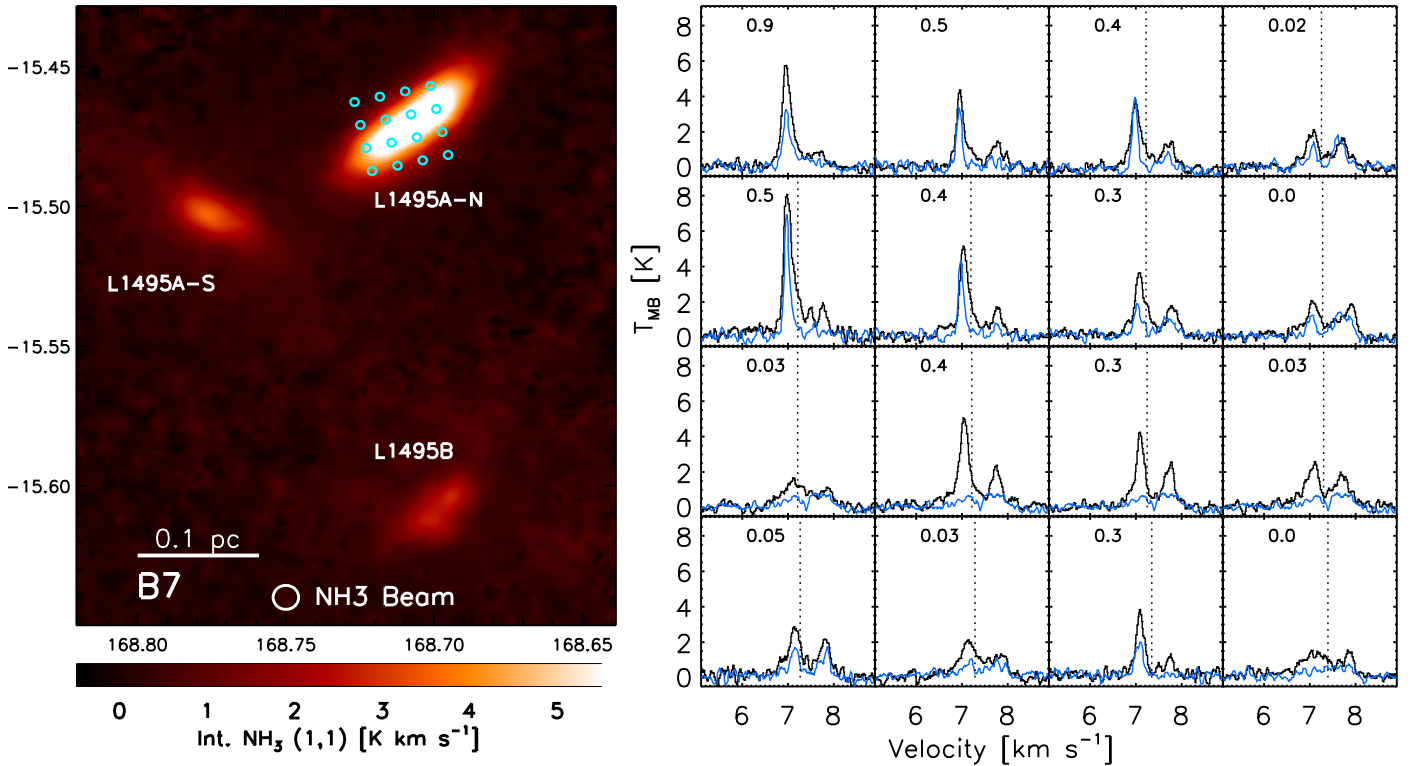


Figure 10. Integrated NH_3 (1,1) (left) and HCN and HCO^+ 1–0 lines observed toward L1495A-N (right). Galactic coordinates are used in the left panel. The 16 small, cyan circles in the left panel denote the beams of Argus, and the corresponding spectra are shown in the right panel with each box corresponding to an Argus beam. The position of the Argus observation is chosen for the 16 beams to cover the core center and its outskirts. HCO^+ 1–0 and HCN $J = 1-0$, $F = 2-1$ are shown as black and blue lines, respectively. The dotted vertical lines present the LSR velocities of the NH_3 emission. The speeds of converging motions evaluated using the two-layer model (Myers et al. 1996) are indicated in each panel in units of km s^{-1} . Only the HCO^+ lines are used for evaluating the speed of converging motions because the signal-to-noise ratio of HCN is insufficient for accurate results.

in the LSR velocities between the Groups II and III is consistent with the speed of converging gas flows measured in HCO^+ , which suggests that L1495A-N and the large-scale ^{13}CO gas are connected in the PPV space. Having a coherent

gas flow from parsec to subparsec scale suggests that the formation and evolution of the L1495A-N core are not determined solely by local dynamics but may be driven by large-scale gas flows.

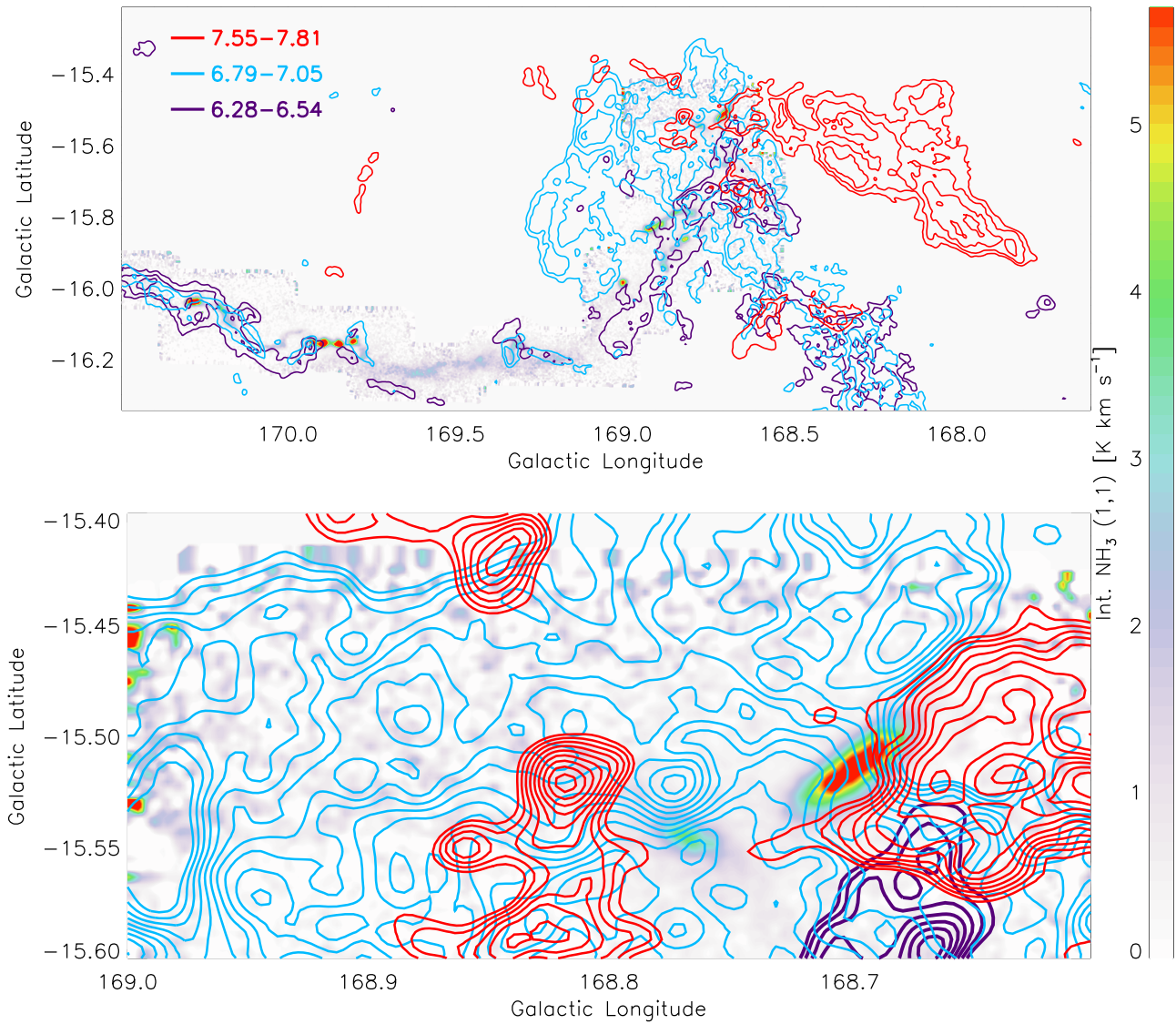


Figure 11. Channel maps of ^{13}CO 1–0 (contours) and integrated intensity maps of NH_3 (1,1) (color) in the L1495-B218 filaments (top) and in L1495A/B7N (bottom). ^{13}CO contours start at 0.44 K km s^{-1} and increase in steps of 0.1 K km s^{-1} for the top panel and in steps of $0.025 \text{ K km s}^{-1}$ for the bottom panel. The velocity range for each channel is written in different color in units of km s^{-1} .

3.3.2. L1521D and B213E

We probe the kinematics of the B213E region containing dense cores L1521D, No.30, No.31, and No.32 using channel maps of CCS and NH_3 (Figure 14). The NH_3 LSR velocity of L1521D is 6.75 km s^{-1} at its center. The blueshifted CCS emission is bright and covers the outskirts of L1521D except for the south side of the core (upper three panels). The redshifted CCS emission is bright at the center and the west side of L1521D (the bottom three panels). The last two panels in Figure 14 show CCS emission near the west side of B213E where there are three NH_3 dense cores (Seo et al. 2015). It shows that the CCS intensity peak coincides with the NH_3 intensity peak of the NH_3 core No.32 in the channel map.

We further investigate the kinematics using the LSR velocity map of B213E in Figure 15. In L1521D, the velocity gradient within L1521D is $3 \text{ km s}^{-1} \text{ pc}^{-1}$ in both NH_3 and CCS, which is similar to the average velocity gradient of fast rotating dense cores (Goodman et al. 1993). In B213E, the LSR velocity changes steeply from the dense core No.31 to the dense core

No.32 with $13 \text{ km s}^{-1} \text{ pc}^{-1}$, which is a considerably larger gradient than a fast rotating core. The transition may be due to either the two cores being at different LSR velocities that overlap at their outskirts or a recent collision with each other.

To see whether L1521D and dense cores No.30, No.31, and No.32 have converging motions, we observed them in HCN 1–0 and HCO^+ 1–0 using the 12 m ARO and the 100 m GBT with Argus. We found that only L1521D shows blue asymmetric profiles in HCO^+ 1–0 and HCN 1–0 (Figures 9, 16). Using a radiative transfer calculation, we evaluated the optical depths of the observed HCN and HCO^+ 1–0 lines and found that they are ≥ 2 , which is similar to the optical depths of other dense cores in HCN and HCO^+ 1–0 (De Vries & Myers 2005; Williams et al. 2006; Campbell et al. 2016). This confirms that the blue asymmetric profiles of HCN 1–0 and HCO^+ 1–0 in L1521D are the self-absorbed features due to a converging motion. The HCN $J = 1-0$ emission of L1521D observed using the 12 m ARO is relatively weak compared to HCO^+ $J = 1-0$ emission (Figure 9). On the other hand, HCO^+ $J = 1-0$ from the 12 m ARO has bright emission

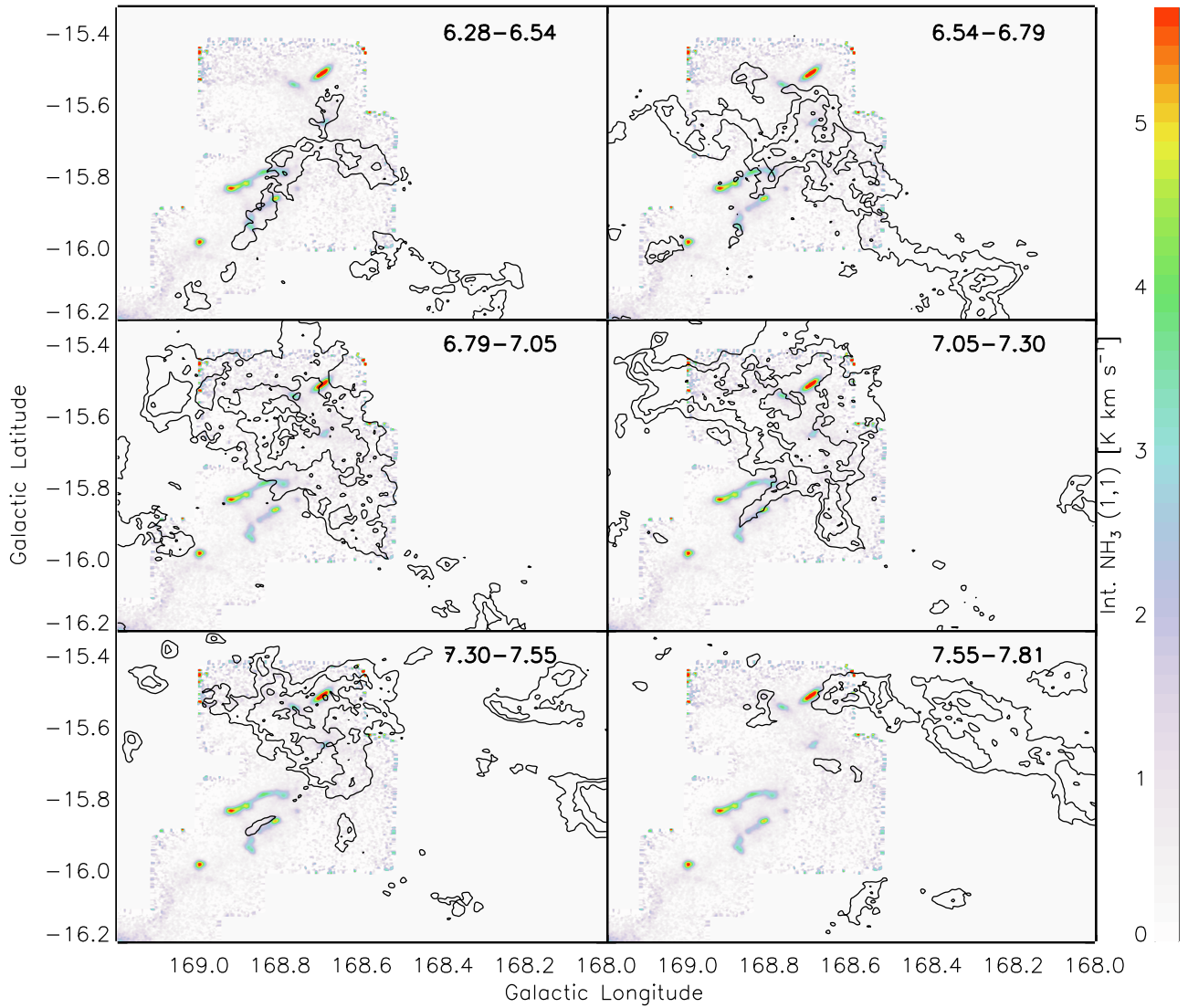


Figure 12. Channel maps of ^{13}CO 1–0 (contours) and integrated intensity maps of NH_3 (1,1) (color) in L1495 and B10. ^{13}CO contours start at 0.5 K km s^{-1} and increase in steps of 0.13 K km s^{-1} . The velocity range for each channel is written in each panel in units of km s^{-1} .

(>1 K) with a blue asymmetric, self-absorbed profile. The estimated converging-motion speed using HCO^+ 1–0 is 0.08 km s^{-1} using the two-layer model (Myers et al. 1996), which is a bit less than half of the sound speed and substantially slower than the speeds measured in L1495A-N.

Observations toward L1521D using the GBT show internal dynamics similar to those found using the 12 m ARO. The position of the observation is chosen to cover the outskirts and the inner region of L1521D. L1521D shows converging-motion signatures on both east and west sides with converging-motion speeds in the range $0.05\text{--}0.1 \text{ km s}^{-1}$. HCN and HCO^+ 1–0 intensities are stronger on the east side of the core, similar to CCS emission, which may be due to an asymmetry in the chemistry or the excitation. The converging-motion speeds measured in HCN and HCO^+ 1–0 are similar on both sides of the core, and no significant asymmetry in the internal dynamics is found. As we shall discuss in Section 4, in terms of the kinematics, L1521D is similar to a slowly contracting core because of self-gravity. As for dense core No.32, mapping using the GBT shows complex line profiles and shows that

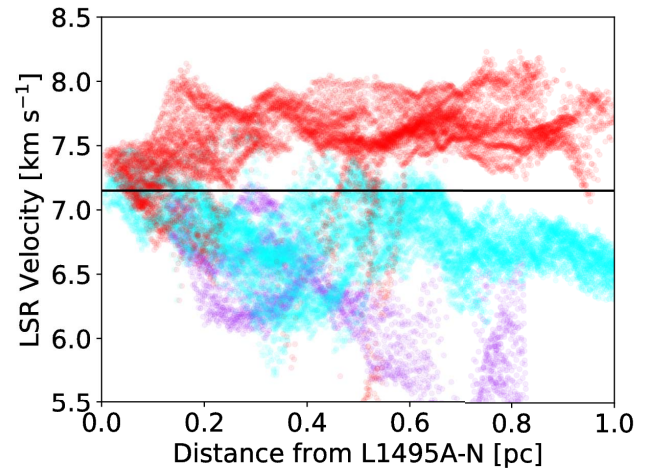


Figure 13. LSR velocities of the brightest ^{13}CO lines along the three groups of CO structures from L1495A-N. The purple, cyan, and red dots represent spectra of Group I, II, and III, respectively, of the CO structures. The LSR velocity is evaluated by fitting a single Gaussian profile to the brightest component in a spectrum. The black horizontal line indicates the LSR velocity of L1495A-N at its center.

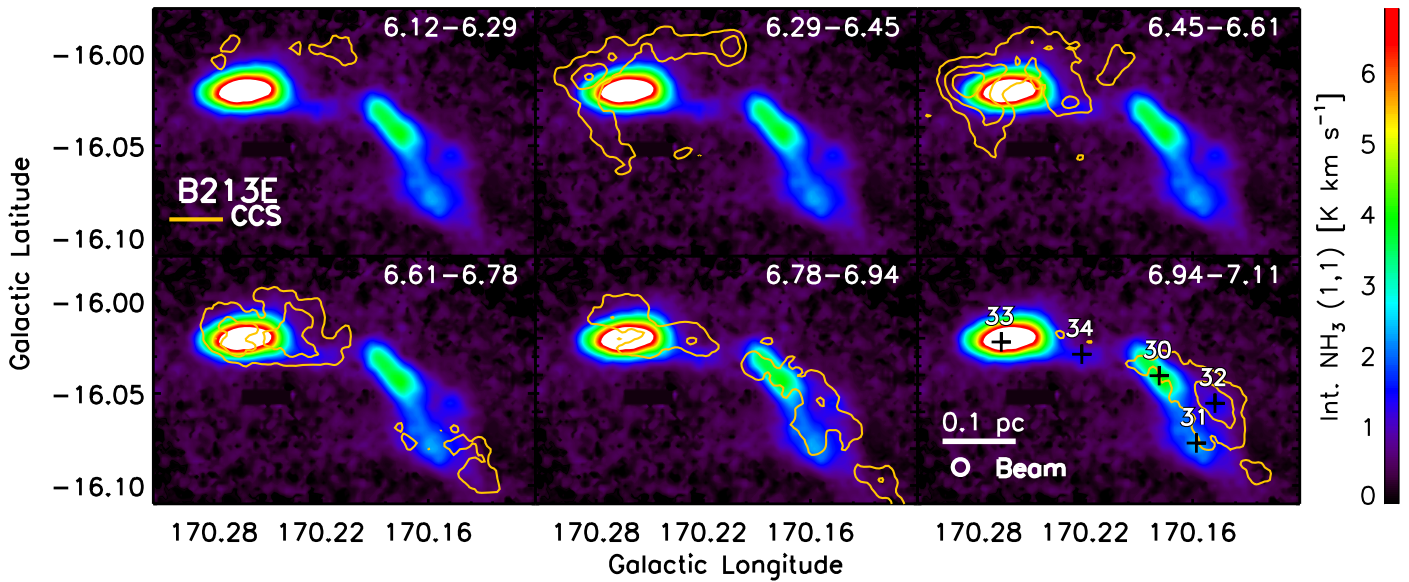


Figure 14. Channel map of CCS (contours) and integrated intensity of NH_3 (1,1) (color) in B213E. CCS contours start from 0.1 K km s^{-1} and increase in steps of 0.1 K km s^{-1} . The velocity range for each channel map is written in each panel in km s^{-1} . The identities of NH_3 dense cores are marked in the last panel.

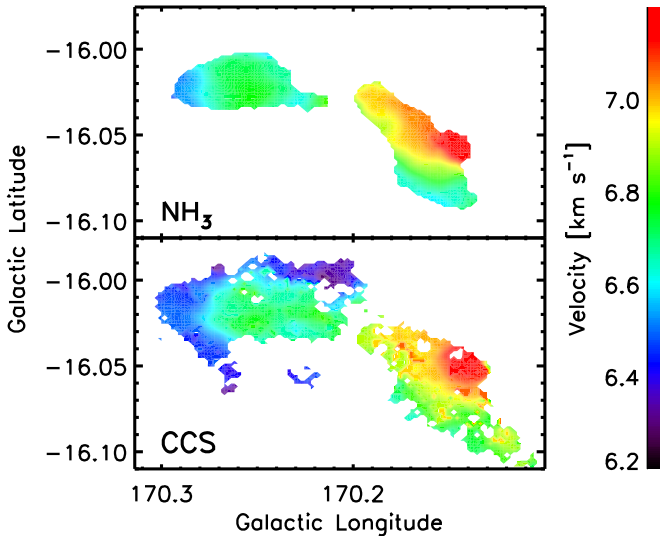


Figure 15. Maps of the NH_3 (top) and CCS (bottom) LSR velocities in B213E.

there are at least three velocity components, but there is no suggestion of a significant converging motion.

To see whether the gas motions in L1521D are connected with large-scale flows, we investigate ^{13}CO and ^{12}CO channel maps together with NH_3 and dust structures in B213E in Figure 17. The velocity ranges of ^{13}CO and ^{12}CO channel maps are chosen to highlight the CO flows, so the redshifted and blueshifted components are not isolated structures but continuous flows in the PPV space. In the region close to L1521D, the ^{13}CO 1–0 emission is redshifted in the south of L1521D and is blueshifted in the north of L1521D. On the other hand, on a large scale, the ^{12}CO 1–0 emission is redshifted in the northwest of L1521D and is blueshifted in the south of L1521D. The CCS and NH_3 flows in L1521D do not have the same direction as the ^{12}CO flows but are seamlessly connected with ^{13}CO in the PPV space. Hence, the gas flow in L1521D is possibly a local flow restricted by the filaments but not connected to the large-scale flows that follow the striations seen

in dust continuum emission (Palmeirim et al. 2013). To the west side of B213E, where three NH_3 cores (No.30, No.31, and No.32) are located, the LSR velocity of CCS changes from the southeast to the northwest direction, a shift that is aligned with the LSR velocities of both ^{12}CO and ^{13}CO .

3.3.3. B216

We investigate the kinematics in the B216 region using the channel maps of CCS compared to the integrated NH_3 (1,1) and dust continuum at $500 \mu\text{m}$ (Figure 18). The CCS emission in B216 spans 6.10 – 6.87 km s^{-1} . The CCS intensity peak does not coincide with NH_3 or dust continuum intensity peaks but is centered 0.08 pc to the southwest from the NH_3 peaks and dust continuum peaks. The two NH_3 dense cores, No.35 and No.36, have LSR velocities of 6.66 and 6.76 km s^{-1} . CCS emission only at 6.6 – 6.8 km s^{-1} is spatially associated with NH_3 cores and dust continuum peak. The CCS peak (also known as L1521B) was previously observed by Hirota et al. (2004) as an example of a CCS-bright young core. Our observations indicate that CCS does not trace the dense core in this region.

4. Discussion

4.1. CCS and HC_7N Chemistry in L1495-B218 Filaments

4.1.1. Our Observations and Previous Studies

The CCS-bright “core” predicted by Suzuki et al. (1992) is rarely found. In surveys of the Taurus molecular cloud (Suzuki et al. 1992; Hirota et al. 2009), CCS is detected in 18 of 29 cores, but only dense core L1521E is confirmed to have a CCS emission peak coinciding with the dust continuum peak (Hirota et al. 2002; Tafalla & Santiago 2004), which indicates that the lifetime of the CCS peak is, at most, 0.04 Myr (the lifetime of a dense core is roughly 1 Myr at the core mean density of $\bar{n}_{\text{H}_2} = 10^4 \text{ cm}^{-3}$; André et al. 2014). The frequency of finding CCS-bright cores would be higher if Suzuki’s chemical model were true for all cores, because CCS is abundant up to 1 Myr in Suzuki’s model.

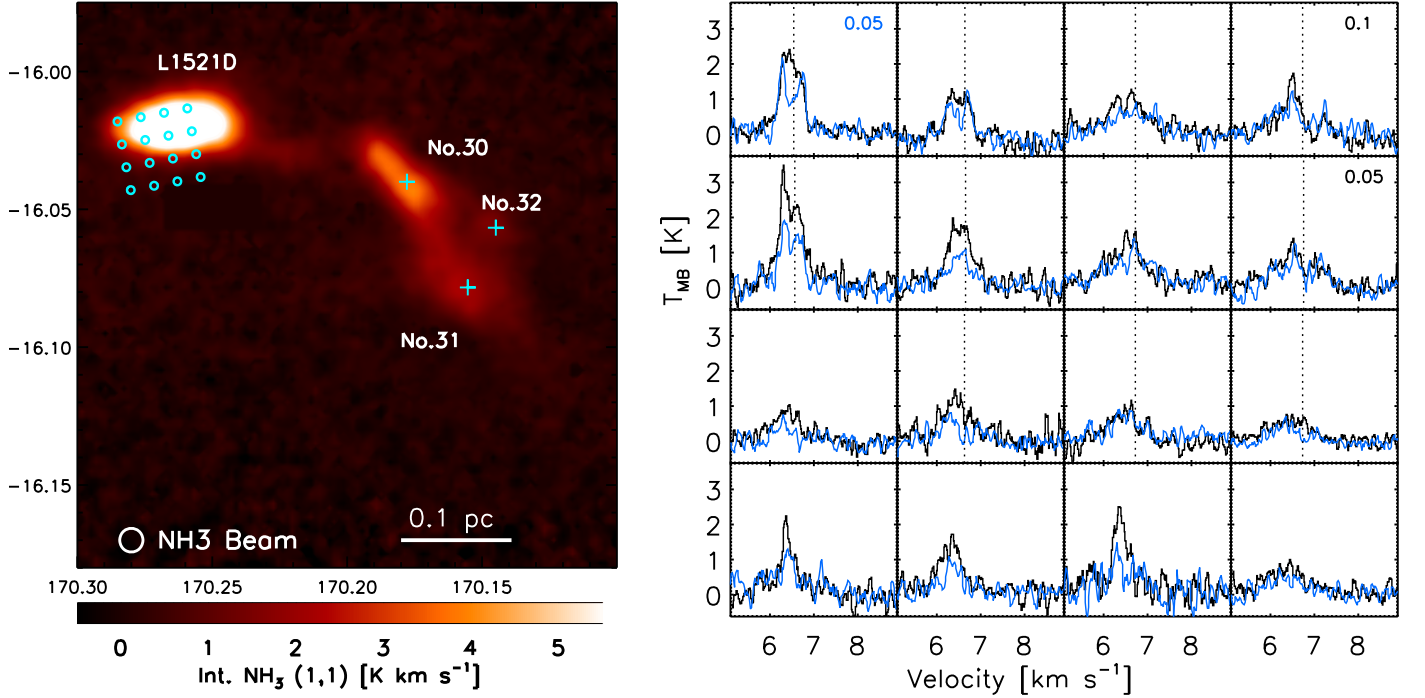


Figure 16. Integrated NH_3 (1,1) (left) and HCN and HCO^+ 1–0 lines observed toward L1521D (right). The Galactic coordinates are used in the left panel. The 16 small, cyan circles in the left panel denote the beams of Argus and the spectra are shown in the right panel. The position of the Argus observation is chosen for the 16 beams to cover the core center as well as its outskirts. The boxes in the right panel correspond to the Argus beams in the left panel. HCO^+ 1–0 and HCN $J = 1-0$, $F = 2-1$ are shown as black and blue lines, respectively. The dotted vertical lines present the LSR velocities of the NH_3 emission. The speeds of converging motions evaluated using the two-layer model (Myers et al. 1996) are written in the unit of km s^{-1} . The speeds evaluated using HCO^+ and HCN lines are written in black and blue, respectively.

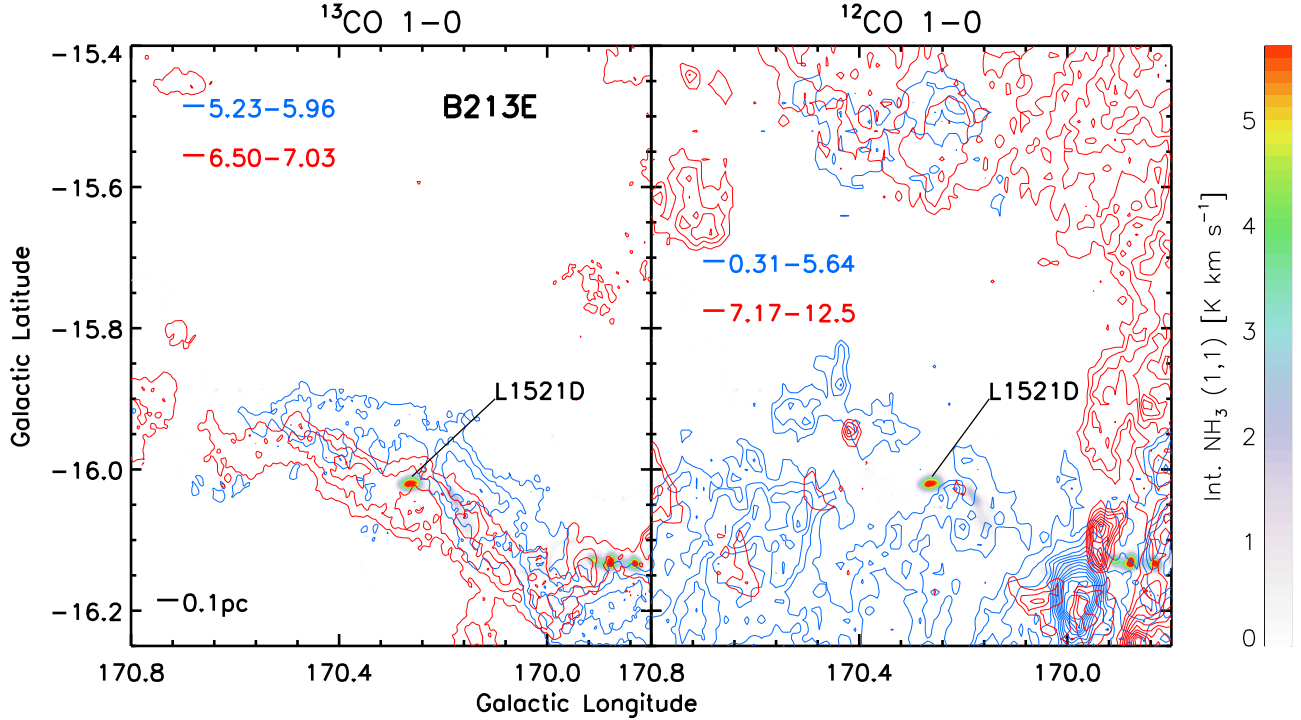


Figure 17. Channel maps of ^{13}CO 1–0 (contours, left) and ^{12}CO 1–0 (contours, right) overlaid on integrated intensity NH_3 (1,1) map in the B213E region. ^{13}CO contours start at 0.75 K km s^{-1} and increase in steps of 0.23 K km s^{-1} . ^{12}CO contours start at 1.5 K km s^{-1} and increase in steps of 0.46 K km s^{-1} . The velocity ranges (in km s^{-1}) are denoted by different colors and indicated in each panels. The velocity range for each channel is written in different color in the unit of km s^{-1} .

We find that CCS is rarely bright at the center of the cores traced by NH_3 or dust continuum, but rather peaks on the core outskirts or outside the cores. Only one core (No.32) of 39 NH_3

cores along the L1495-B218 filaments has a good agreement among the dust, NH_3 , and CCS intensity peaks. Thus, there are only two dense cores (No.32 and L1521E) in the Taurus

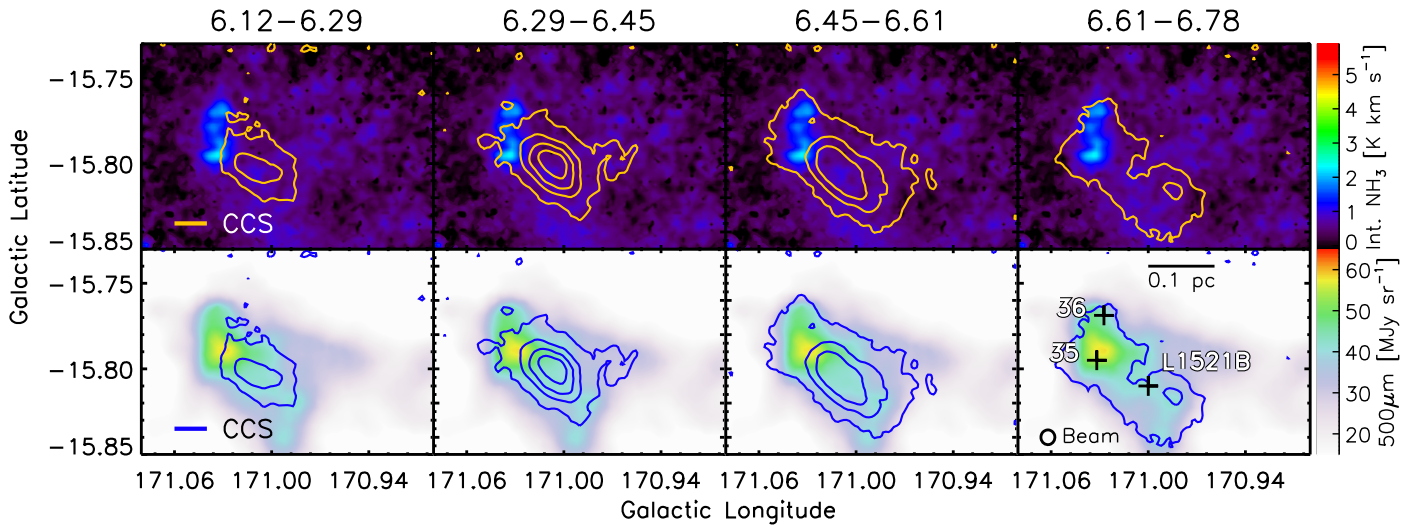


Figure 18. Channel map of CCS (contours) and integrated intensity of NH_3 (1,1) (color) in B216. CCS contours start at 0.03 K km s^{-1} and increase in steps of 0.11 K km s^{-1} . The velocity range in km s^{-1} for each channel map is written above each column.

molecular cloud known to have coincident CCS and dust continuum intensity peaks. In particular, CCS emission in B216, which contains only young dense cores with no star formation activity, clearly shows that CCS intensity peaks do not coincide with NH_3 or dust continuum peaks (L1521B), even at an early evolutionary stage. This suggests that CCS is not a good tracer with which to trace core density structure.

We found that CCS emission is detected in both less-evolved regions (B216 and B211) and the more-evolved regions with star formation activity (L1495A/B7N and B213E), whereas we did not detect any significant CCS emission in B213W and B10, which seem to be at evolutionary stages slightly younger or similar to those of L1495A/B7N and B213E (Seo et al. 2015). Comparing the column density among the starless cores, we find that two more-condensed starless cores (e.g., L1521D and L1495A-N) have the brightest CCS and HC_7N emission, whereas some other starless cores at the similar column density (e.g., starless cores in B213W) have no significant CCS and HC_7N detection at our noise level. We also find that the less-condensed starless cores and filaments in our survey (e.g., starless cores in B216 and filaments in B211) have CCS emission but no HC_7N emission. In the moderately condensed starless cores in B10, we could not detect significant CCS or HC_7N emission. In summary, our CCS survey toward the L1495-B218 filaments shows that there is significant CCS emission in the less-condensed starless cores and filaments but also occasionally in more-condensed starless cores. This is not consistent with the prediction of the Suzuki model, which predicts that most of the starless cores in Taurus should have significant CCS emission.

Aikawa et al. (2001) made a chemical model of a dense core considering grain-surface chemistry and collapse dynamics. They demonstrated that the CCS abundance is more sensitive to the absolute age of the cores than to the gas density, suggesting that a more-condensed core can have a high CCS abundance if it is young. For example, L1544 and L1689B have similar densities and show signatures of converging-motion, but L1689B has considerably brighter CCS emission than does L1544. This may be because L1689B may be younger or has accreted surrounding gas more recently than has L1544 (Lee et al. 2003; Sohn et al. 2007; Seo et al. 2013). Although Aikawa’s model suggests a possibility of having high CCS abundance in more-condensed

starless cores, it still predicts considerably more CCS-bright cores than our observations and is relatively similar to Suzuki’s model. This may be because the physical and chemical conditions of L1495-B218 filaments are different from Aikawa’s model and because their chemical network including both gas and grain-surface chemistry is relatively simple. In this study, we evaluate chemical evolution in the L1495-B218 filaments using a state-of-the-art astrochemistry code using the observed physical conditions in Taurus.

4.1.2. Chemistry of Typical Starless Cores in the L1495-B218 Filaments

We modeled the chemistry in dense cores in Taurus using the state-of-the-art chemical code NAUTILUS (Ruaud et al. 2016). It simulates a three-phase chemistry, including gas-phase, grain-surface, and grain-mantle chemistry, where both surface and the mantle are chemically active with possible exchanges between the different phases. Adsorption of gas-phase species onto grain surfaces, the thermal and nonthermal desorption of species from the grain surface into the gas phase, and species from the surface to mantle and mantle to the surface are the primary exchange processes. This chemical code considers the latest updates on various physico-chemical processes from the KIDA database¹¹ which is more advanced than previous studies reported in Suzuki et al. (1992) and Aikawa et al. (2001). NAUTILUS has been tested, benchmarked, and applied to multiple cases, including dense cores (Majumdar et al. 2017b; Vidal et al. 2017), low-mass protostellar envelopes (Majumdar et al. 2017a, 2018a), hot cores (Vidal & Wakelam 2018), and protoplanetary disks (Wakelam et al. 2016). The gas-phase chemistry of NAUTILUS is based on the public chemical network kida.uva.2014 (Wakelam et al. 2015) with updates for sulfur chemistry (Vidal et al. 2017) and the chemistry of complex organics (Majumdar et al. 2018b) from the KIDA database, whereas surface reactions are based on Garrod (2008) with additional updates from Ruaud et al. (2016), Vidal et al. (2017), and Majumdar et al. (2018b). Using NAUTILUS, we explored a wide range of parameters, including density, temperature, visual extinction, and initial elemental abundances

¹¹ <http://kida.obs.u-bordeaux1.fr/>

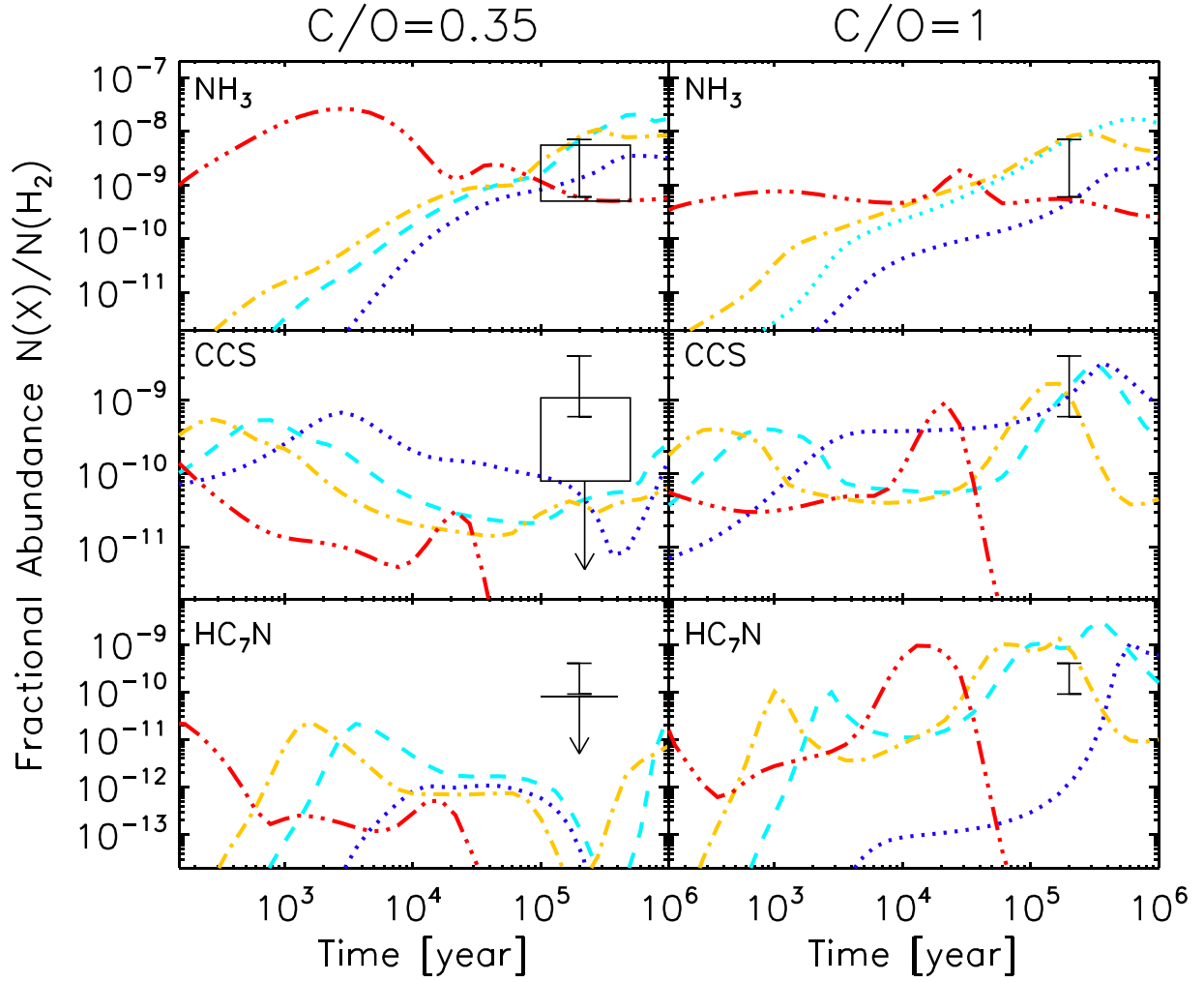


Figure 19. Fractional abundances of NH_3 , CCS , and HC_7N with respect to H_2 as a function of time. The blue dotted, cyan dashed, orange dashed-dotted, and red dashed-triple dotted lines denote densities at $n_{\text{H}_2} = 4 \times 10^3$, 2×10^4 , 5×10^4 , and $5 \times 10^5 \text{ cm}^{-3}$, respectively. The chemical models with the initial gas-phase C/O ratio of 0.35 (left column) have good agreement with most of the regions in L1495-B218 filaments except L1495A-N and L1521D. The chemical models with C/O ratio of 1 (right column) show relatively more abundant CCS and HC_7N than do the other models and better match the CCS and HC_7N abundances in L1495A-N and L1521D. The black boxes show ranges of the observed fractional abundances in starless cores except L1495A-N and L1521D. The arrows denote nondetection of CCS and HC_7N in B10 and B213W. The bar plots denote ranges of the fractional abundances in L1495A-N and L1521D.

to model the chemistry in different environments. We limited excessive complexity of three-phase physio-chemical modeling by assuming that there is no inflow to the cores.

We use the following model parameters to represent the chemical evolution of CCS , NH_3 , and HC_7N in the majority of starless cores in the L1495-B218 filaments.

1. High-density core: $T = 8 \text{ K}$; $n_{\text{H}_2} = 5 \times 10^5 \text{ cm}^{-3}$; $A_V = 20 \text{ mag}$
2. Mid-density core: $T = 10 \text{ K}$; $n_{\text{H}_2} = 5 \times 10^4 \text{ cm}^{-3}$; $A_V = 15 \text{ mag}$
3. Low-density core: $T = 10 \text{ K}$; $n_{\text{H}_2} = 2 \times 10^4 \text{ cm}^{-3}$; $A_V = 8 \text{ mag}$
4. Core outskirts: $T = 15 \text{ K}$; $n_{\text{H}_2} = 4 \times 10^3 \text{ cm}^{-3}$; $A_V = 3 \text{ mag}$.

The densities are chosen from the average density along the lines of sight to the starless cores in the L1495-B218 filaments. The extinction values are directly estimated from the Schmalzl et al. (2010) observations. The temperature values are adopted from the kinetic temperature of the starless cores estimated using NH_3 (Seo et al. 2015).

The selection of the set of initial gas-phase elemental abundances in the chemical models is not a trivial task because the abundances of the elements strongly influence the chemical state of the gas (Agúndez & Wakelam 2013). A prime example is the relative amount of carbon and oxygen, which is known to strongly affect the chemistry (Le Bourlot et al. 1995; van Dishoeck & Blake 1998). To reflect the large uncertainties in the gas-phase elemental abundances of carbon and oxygen, the range of carbon-to-oxygen gas-phase elemental abundance ratio (noted C/O hereafter) is often varied between 0.3 and 1.5 (Cartledge et al. 2004; Le Gal et al. 2014). The elemental gas-phase abundance of sulfur is also very poorly constrained and we have yet to locate the main reservoir of sulfur in the interstellar matter (ISM) (Majumdar et al. 2017a; Vidal & Wakelam 2018). The range of initial sulfur abundances can vary by almost three orders of magnitude if we consider the range determined by the so-called low metal and high metal abundances defined by Graedel et al. (1982).

Here, we first show chemical models with an initial C/O elemental ratio of 0.35, which is close to the solar value (Le Gal et al. 2014). The initial sulfur abundance in the models is

Table 1

The Main Production and Destruction Reactions with Their Relative Contributions for NH₃, CCS, and HC₇N at Different Ages for Mid-density Core Outskirts ($4 \times 10^3 \text{ cm}^{-3}$) Models with Initial C/O = 0.35

Density cm^{-3}	Age yr	Species	Formation	Destruction
4×10^3	10^2	NH ₃	$\text{NH}_4^+ + \text{e}^- \rightarrow \text{H} + \text{NH}_3$ (69.2%) $\text{H-ice} + \text{NH}_2\text{-ice} \rightarrow \text{NH}_3$ (30.2%)	$\text{NH}_3 + \text{C}^+ \rightarrow \text{H} + \text{HCNH}^+$ (62.9%) $\text{NH}_3 + \text{C}^+ \rightarrow \text{C} + \text{NH}_3^+$ (31.5%)
		CCS	$\text{HC}_2\text{S}^+ + \text{e}^- \rightarrow \text{H} + \text{CCS}$ (89.2%) $\text{HC}_3\text{S}^+ + \text{e}^- \rightarrow \text{CH} + \text{CCS}$ (8.4%)	$\text{CCS} + \text{C}^+ \rightarrow \text{S}^+ + \text{C}_3$ (68.7%) $\text{CCS} + \text{C}^+ \rightarrow \text{C} + \text{C}_2\text{S}^+$ (19.6%)
		HC ₇ N	$\text{N} + \text{C}_7\text{H}^- \rightarrow \text{HC}_7\text{N} + \text{e}^-$ (41%) $\text{CN} + \text{C}_6\text{H}_2 \rightarrow \text{H} + \text{HC}_7\text{N}$ (35.6%)	$\text{HC}_7\text{N} + \text{C}^+ \rightarrow \text{H} + \text{C}_8\text{N}^+$ (49.7%) $\text{HC}_7\text{N} + \text{C}^+ \rightarrow \text{CN} + \text{C}_7\text{H}^+$ (49.7%)
		NH ₃	$\text{H-ice} + \text{NH}_2\text{-ice} \rightarrow \text{NH}_3$ (69.9%) $\text{NH}_4^+ + \text{e}^- \rightarrow \text{H} + \text{NH}_3$ (29.4%)	$\text{NH}_3 + \text{S}^+ \rightarrow \text{S} + \text{NH}_3^+$ (34%) $\text{NH}_3 + \text{C}^+ \rightarrow \text{H} + \text{HCNH}^+$ (20.5%)
		CCS	$\text{HC}_2\text{S}^+ + \text{e}^- \rightarrow \text{H} + \text{CCS}$ (50.4%) $\text{C} + \text{HCS} \rightarrow \text{CCS} + \text{H}$ (28.4%)	$\text{CCS} + \text{O} \rightarrow \text{CO} + \text{CS}$ (61.6%) $\text{CCS} + \text{C} \rightarrow \text{C}_2 + \text{CS}$ (30.3%)
		HC ₇ N	$\text{N} + \text{C}_8\text{H} \rightarrow \text{HC}_7\text{N} + \text{C}$ (85.4%) $\text{C}_7\text{H}_2\text{N}^+ + \text{e}^- \rightarrow \text{H} + \text{HC}_7\text{N}$ (8%)	$\text{HC}_7\text{N} + \text{C} \rightarrow \text{H} + \text{C}_8\text{N}$ (47.3%) $\text{HC}_7\text{N} + \text{H}^+ \rightarrow \text{H} + \text{HC}_7\text{N}^+$ (16.1%)
	10^6	NH ₃	$\text{NH}_4^+ + \text{e}^- \rightarrow \text{H} + \text{NH}_3$ (96.5%) $\text{H-ice} + \text{NH}_2\text{-ice} \rightarrow \text{NH}_3$ (3.1%)	$\text{NH}_3 + \text{H}^+ \rightarrow \text{H} + \text{NH}_3^+$ (27.2%) $\text{NH}_3 + \text{h}\nu \rightarrow \text{H} + \text{NH}_2$ (21.5%)
		CCS	$\text{HC}_2\text{S}^+ + \text{e}^- \rightarrow \text{H} + \text{CCS}$ (58%) $\text{S} + \text{CCH} \rightarrow \text{H} + \text{CCS}$ (37.1%)	$\text{CCS} + \text{H}^+ \rightarrow \text{H} + \text{C}_2\text{S}^+$ (61%) $\text{CCS} + \text{H}_3^+ \rightarrow \text{H}_2 + \text{HC}_2\text{S}^+$ (10%)
		HC ₇ N	$\text{CN} + \text{C}_6\text{H}_2 \rightarrow \text{H} + \text{HC}_7\text{N}$ (47.6%) $\text{C}_7\text{H}_2\text{N}^+ + \text{e}^- \rightarrow \text{H} + \text{HC}_7\text{N}$ (40.4%)	$\text{HC}_7\text{N} + \text{H}^+ \rightarrow \text{H} + \text{HC}_7\text{N}^+$ (41.5%) $\text{HC}_7\text{N} + \text{H}_3^+ \rightarrow \text{H}_2 + \text{C}_7\text{H}_2\text{N}^+$ (49.7%)

5×10^{-7} with respect to hydrogen nuclei, whereas the solar value is 1.5×10^{-5} . Thus, we have applied a depletion factor (defined by the ratio of solar to adopted value in the model) of 30 from the gas phase, which is smaller than the best-fit depletion factor of 200 adopted to reproduce the observations of different sulfur-bearing species in L1544 prestellar core by Vastel et al. (2018). They also discussed the variation of sulfur depletion for different sources. We find that the initial sulfur abundance of 5×10^{-7} results in the best fits to the observed fractional abundances in the L1495-B218 filaments.

Figure 19 shows the fractional abundance profiles of NH₃, CCS, and HC₇N as a function of time. By running a grid of chemical models, we find that the chemical models with C/O = 0.35 provide the best fit to our observations, except for L1495A-N and L1521D, because the models and observations have good agreement within a factor of five. We consider a factor of five as the reasonable uncertainty between the models and the observations because the uncertainties of the observed fractional abundances are typically a factor of three. The uncertainties of the NH₃ fractional abundance are mostly in the H₂ column density because of uncertainty in the dust properties, whereas the column densities of NH₃ have uncertainties typically lower than 30% as a result of a high S/N ratio. The column densities of HC₇N and CCS depend on the excitation temperature. If the excitation temperature is 6 K, the column density will be 30% higher than a case when $T_k = T_{\text{ex}}$, whereas it can be three times higher if $T_{\text{ex}} = 4$ K. Because we have not observed other transitions of CCS and HC₇N, we could not measure the excitation temperature. A typical excitation temperature of CCS 2₁–1₀ measured in Taurus is around 6 K (Suzuki et al. 1992; Wolkovitch et al. 1997; Vastel et al. 2018). The excitation temperature of HC₇N 21–20 is not measured in Taurus.

In this subsection, we will first discuss our chemical models with C/O = 0.35 and compare the models to our observations, except for the two dense cores, L1495A-N and L1521D, observed to have converging-motion signatures. We will elaborate on these two dense cores in the following subsection because they show significantly different chemical characteristics compared to the other starless cores in the L1495-B218 filaments.

The general trend of the fractional abundances of NH₃, CCS, and HC₇N in the models with C/O = 0.35 show evolution similar to that in Aikawa’s models with small differences in details. The main chemical channels for forming and destroying NH₃, CCS, and HC₇N are given in Tables 1 and 2 for the core outskirts and mid-density core models. The fractional abundance of NH₃ increases almost monotonically as a function of time, except for the high-density core model (see Figure 19). In the high-density model, the NH₃ fractional abundance decreases after 3×10^3 yr because of depletion onto dust grains. The peak NH₃ abundance is lower when the gas density is higher, because the depletion of NH₃ onto the dust grain surface becomes more efficient at the high-density core model, which is also observed in Aikawa’s model. The fractional abundance of CCS shows a more-complicated evolution compared to NH₃ with three different trends as a function of time: a rapid increase of the fractional abundance at early times ($< a \text{ few } 1000 \text{ yr}$), a decrease of the fractional abundance from $\sim 10^{-9}$ to 10^{-11} from ~ 1000 yr to $\sim 0.1 \text{ Myr}$, and a slow increase of the abundance again after $\sim 0.1 \text{ Myr}$. The decrease of the CCS abundance is mainly due to its destruction by oxygen in gas-phase and is not due to depletion on dust grains (Table 1 and Table 2), unlike other carbon-bearing species (e.g., Tafalla & Santiago 2004; Pagani et al. 2005). The slow increase in CCS after $\sim 0.1 \text{ Myr}$ is because its destruction rate by oxygen is significantly reduced as a result of the depletion

Table 2

The Main Production and Destruction Reactions with Their Relative Contributions for NH₃, CCS and HC₇N at Different Ages for Mid-density Core ($5 \times 10^4 \text{ cm}^{-3}$) Models with Initial C/O = 0.35

Density cm^{-3}	Age yr	Species	Formation	Destruction
5×10^4	10^2	NH ₃	H-ice + NH ₂ -ice \rightarrow NH ₃ (92%) NH ₄ ⁺ + e ⁻ \rightarrow H + NH ₃ (7.9%)	NH ₃ + C ⁺ \rightarrow H + HCNH ⁺ (61.9%) NH ₃ + C ⁺ \rightarrow C + NH ₃ ⁺ (31%)
		CCS	HC ₂ S ⁺ + e ⁻ \rightarrow H + CCS (78.2%) HC ₃ S ⁺ + e ⁻ \rightarrow CH + CCS (17.1%)	CCS + C ⁺ \rightarrow S ⁺ + C ₃ (65.7%) CCS + C ⁺ \rightarrow C + C ₂ S ⁺ (18.8%)
		HC ₇ N	N + C ₇ H ⁻ \rightarrow HC ₇ N + e ⁻ (56.8%) CN + C ₆ H ₂ \rightarrow H + HC ₇ N (20.6%)	HC ₇ N + C ⁺ \rightarrow H + C ₈ N ⁺ (48.4%) HC ₇ N + C ⁺ \rightarrow CN + C ₇ H ⁺ (48.4%)
	10^5	NH ₃	NH ₄ ⁺ + e ⁻ \rightarrow H + NH ₃ (95.7%) H-ice + NH ₂ -ice \rightarrow NH ₃ (3.3%)	NH ₃ + H ₃ ⁺ \rightarrow H ₂ + NH ₄ ⁺ (25.2%) NH ₃ + H ₃ O ⁺ \rightarrow H ₂ O + NH ₄ ⁺ (24.3%)
		CCS	HC ₂ S ⁺ + e ⁻ \rightarrow H + CCS (62.2%) HC ₃ S ⁺ + e ⁻ \rightarrow CH + CCS (15.3%)	CCS + O \rightarrow CO + CS (90.2%) CCS + N \rightarrow CN + CS (2.3%)
		HC ₇ N	N + C ₈ H \rightarrow HC ₇ N + C (45%) C ₇ H ₂ N ⁺ + e ⁻ \rightarrow H + HC ₇ N (44.5%)	HC ₇ N + H ₃ ⁺ \rightarrow H ₂ + C ₇ H ₂ N ⁺ (49.4%) HC ₇ N + HCO ⁺ \rightarrow CO + C ₇ H ₂ N ⁺ (24.8%)
	10^6	NH ₃	NH ₄ ⁺ + e ⁻ \rightarrow H + NH ₃ (99.5%)	NH ₃ + H ₃ ⁺ \rightarrow H ₂ + NH ₄ ⁺ (76.2%) NH ₃ + H ⁺ \rightarrow H + NH ₃ ⁺ (10.6%)
		CCS	HC ₂ S ⁺ + e ⁻ \rightarrow H + CCS (73%) S + CCH \rightarrow H + CCS (14.8%)	CCS + H ₃ ⁺ \rightarrow H ₂ + HC ₂ S ⁺ (79.9%) CCS + H ⁺ \rightarrow H + C ₂ S ⁺ (11.5%)
		HC ₇ N	C ₇ H ₂ N ⁺ + e ⁻ \rightarrow H + HC ₇ N (53.1%) CN + C ₆ H ₂ \rightarrow H + HC ₇ N (45.5%)	HC ₇ N + H ₃ ⁺ \rightarrow H ₂ + C ₇ H ₂ N ⁺ (81.7%) HC ₇ N + H ⁺ \rightarrow H + HC ₇ N ⁺ (11.9%)

of oxygen on dust grains. At this stage, the formation rate of CCS is still relatively low, so the CCS abundance does not rapidly increase as it does at earlier times. HC₇N also shows chemical trends similar to CCS except at low density, where the HC₇N formation via $\text{N} + \text{C}_8\text{H} \rightarrow \text{C} + \text{HC}_7\text{N}$ is much slower than CCS.

We compared our observations to the chemical models with the initial gas-phase C/O = 0.35 in Figure 19. We found that most regions, including B10, B213W, B211, B216, and B218, show good agreement with the models. For example, young and relatively less-condensed starless cores in B211 and B216 have NH₃ fractional abundance $\sim 1 \times 10^{-9}$ with respect to H₂ at the core centers and have CCS fractional abundances of $(0.4\text{--}1) \times 10^{-9}$ with respect to H₂ at CCS peak-intensity positions. Considering the uncertainties in the fractional abundances, we found that B211 and B216 have better agreement with the core outskirts model. From this model, fractional abundances of NH₃ and CCS are 2.2×10^{-9} and 3×10^{-10} , respectively, with respect to H₂ at a chemical age of ~ 0.1 Myr, which is reasonable for young starless cores. The HC₇N abundance at this chemical age is 1×10^{-12} with respect to H₂ which explains our nondetection as well. The NH₃ and CCS abundances in B211 are well-reproduced by our models. For B216, NH₃ is in good agreements with the model at 0.1 Myr, but CCS is a factor of five higher compared to the models at the same age.

Starless cores in B10 and B213W, which are more condensed than the ones in B211 and B216, have fractional abundances of NH₃ of 3×10^{-9} and 5×10^{-9} , respectively, at their centers and 1×10^{-9} and 2×10^{-9} , respectively, at their outskirts. Considering the uncertainties in the fractional abundances, we think that these two regions may

correspond to a chemical age around 0.3 Myr or older, where the CCS fractional abundance steeply decreases in core outskirts models. At this age, the NH₃ abundance is $(1\text{--}20) \times 10^{-9}$ depending on density, whereas the CCS abundance is $(0.1\text{--}2) \times 10^{-10}$ with respect to H₂, which mostly falls below the lowest detected fractional abundance of CCS of 4×10^{-10} . We did not detect HC₇N in B10 and B213W, and the fractional abundance of HC₇N in the model is $\sim 10^{-12}$ or lower, which is below the lowest observed fractional abundance of 5×10^{-11} in our entire HC₇N survey.

Starless cores in B218 are more-condensed cores similar to those in B10 and B213W. These starless cores show weak CCS rings, whereas we did not detect any HC₇N emission at our noise level. The NH₃ fractional abundance ranges are $(3\text{--}4) \times 10^{-9}$ at the core centers. The NH₃ and CCS fractional abundances are $(0.5\text{--}1) \times 10^{-9}$ and $(3\text{--}6) \times 10^{-10}$, respectively, at the outskirts. Comparing these abundances to the mid-density and outskirts models with the initial C/O = 0.35, we found that these starless cores may be at a chemical age between 0.1 Myr and 0.2 Myr. At this age, the mid-density and outskirts models with the initial C/O = 0.35 show the NH₃ and CCS fractional abundance ranges of $(0.8\text{--}10) \times 10^{-9}$ and $(0.5\text{--}1) \times 10^{-10}$, respectively, and are in good agreement with the observed abundances.

We found that most of the regions in the L1495-B218 filaments agree with the chemical models with C/O = 0.35. However, we found that two starless cores, L1495A-N and L1521D, have significantly different characteristics compared to other starless cores in Taurus. In the following section, we elaborate chemical evolution of L1495A-N and L1521D and the implications related to their dynamics.

Table 3

The Main Production and Destruction Reactions with Their Relative Contributions for NH₃, CCS, and HC₇N at the Age between 0.2 and 0.4 Myr for Core Outskirts and Mid-density Core Models with Initial C/O = 1

Density cm ⁻³	Species	Formation	Destruction
4×10^3	NH ₃	H-ice + NH ₂ -ice → NH ₃ (90.4%) NH ₄ ⁺ + e ⁻ → H + NH ₃ (9.5%)	NH ₃ + C ⁺ → H + HCNH ⁺ (40.2%) NH ₃ + C ⁺ → C + NH ₃ ⁺ (20.1%)
	CCS	HC ₂ S ⁺ + e ⁻ → H + CCS(68.9%) HC ₃ S ⁺ + e ⁻ → CH + CCS(27.1%)	CCS + C ⁺ → S ⁺ + C ₃ (41.4%) CCS + C → C ₂ + CS(25.8%)
	HC ₇ N	N + C ₈ H → C + HC ₇ N(68.6%) CN + C ₆ H ₂ → H + HC ₇ N(22%)	HC ₇ N + C ⁺ → H + C ₈ N ⁺ (32.9%) HC ₇ N + C ⁺ → CN + C ₇ H ⁺ (32.9%)
5×10^4	NH ₃	NH ₄ ⁺ + e ⁻ → H + NH ₃ (98.6%)	NH ₃ + H ₃ ⁺ → H ₂ + NH ₄ ⁺ (63.7%) NH ₃ + HCO ⁺ → CO + NH ₄ ⁺ (7%)
	CCS	HC ₂ S ⁺ + e ⁻ → H + CCS(63%) S + CCH → H + CCS(20.2%)	CCS + H ₃ ⁺ → H ₂ + HC ₂ S ⁺ (71.2%) CCS + H ⁺ → H + C ₂ S ⁺ (7.6%)
	HC ₇ N	C ₇ H ₂ N ⁺ + e ⁻ → H + HC ₇ N(50.9%) CN + C ₆ H ₂ → H + HC ₇ N(44.7%)	HC ₇ N + H ₃ ⁺ → H ₂ + C ₇ H ₂ N ⁺ (76.7%) HC ₇ N + H ⁺ → H + HC ₇ N ⁺ (8.2%)

4.1.3. Chemistry of L1495A-N and L1521D

The physical conditions of L1495A-N and L1521D, including density structures, extinction at the core surface, kinetic temperature, and turbulence, are similar to those of the starless cores in B213W and B10, but the fractional abundances of CCS and HC₇N in L1495A-N and L1521D are much higher than in the starless cores in B213W and B10.

The fractional abundances of NH₃ and CCS with respect to H₂ at the core centers (NH₃ peak-intensity position) are 4×10^{-9} and 6×10^{-10} , respectively, for L1495A-N, and 5×10^{-9} and 3×10^{-10} , respectively, for L1521D. We did not detect any HC₇N at the core centers. At the CCS peak-intensity position at the outskirts of the cores, the fractional abundances of NH₃ and CCS with respect to H₂ are 3×10^{-10} and 3×10^{-9} , respectively, for L1495A-N, and 5×10^{-10} and 2×10^{-9} , respectively, for L1521D. We did not detect HC₇N emission at these positions. On the other hand, at the HC₇N peak-intensity position, the fractional abundances of NH₃, CCS, and HC₇N with respect to H₂ are 6×10^{-10} , 1×10^{-9} , and 2×10^{-10} , respectively, for L1495A-N and 2×10^{-9} , 1×10^{-9} , and 3×10^{-10} , respectively, for L1521D.

For L1495A-N and L1521D, we found that the models with $n_{\text{H}_2} = 4 \times 10^3 \text{ cm}^{-3}$ and $5 \times 10^4 \text{ cm}^{-3}$ correspond to the average densities in the core outskirts and the core center, respectively, evaluated by column density/size. The actual volume densities of the core centers may be several times higher than $5 \times 10^4 \text{ cm}^{-3}$ but still less than $5 \times 10^5 \text{ cm}^{-3}$ if their density profiles are similar to the Bonnor–Ebert sphere (Ebert 1955; Bonnor 1956). Comparing the observed NH₃ and CCS abundances to the models with the initial C/O = 0.35, we found that the observed CCS fractional abundances of L1495A-N and L1521D are significantly higher (at least 20 times more abundant at core center and at the CCS peak-intensity position) than the models with the initial C/O = 0.35 if we determine the age of the cores using the observed NH₃ abundance to be ~ 0.1 Myr. Also, the peak CCS abundances in the models are still more than five times lower compared to the observed CCS fractional abundance at the CCS peak-intensity positions of L1495A-N and L1521D. We found that the observed HC₇N fractional abundances at the HC₇N

peak-intensity position are at least 100 times higher than the fractional abundance predicted by the model with the initial C/O = 0.35. These discrepancies between the observed fractional abundances and the models with the initial C/O = 0.35 strongly suggest that the two cores are going through a different chemical evolutionary path compared to the other starless cores in the L1495-B218 filaments.

Tables 1 and 2 clearly show the importance of the O + CCS → CO + CS reaction that controls the chemistry of CCS in the majority of starless cores in the L1495-B218 filaments described in an earlier subsection. By running a grid of chemical models, we found that the reaction O + CCS → CO + CS is highly sensitive to the initial gas-phase C/O ratio because the abundance of the gas-phase atomic oxygen controls the reaction flux of this channel (i.e., the higher the C/O ratio, the lower the rate of destruction of CCS). To explain the observed high abundances of CCS together with HC₇N within a reasonable uncertainty, we have found the best agreement to be with the chemical models having C/O = 1.

The right column of Figure 19 shows the evolution of the fractional abundances as a function of time. The general trend of the NH₃ fractional abundance over time in the C/O = 1 models is similar to that of the C/O = 0.35 models. On the other hand, the evolution of the CCS and HC₇N fractional abundances in the C/O = 1 models is very different from the C/O = 0.35 models. The CCS and HC₇N fractional abundances in the C/O = 1 models are significant even at an age of >1 Myr, having peak abundances $>10^{-9}$, whereas the CCS and HC₇N fractional abundances in the C/O = 0.35 models tend to decrease and maintain an abundance of $<10^{-10}$ over a long period of time after a few times 0.01 Myr. This is mainly because of less oxygen being available to destroy CCS and more carbon to form CCS and HC₇N when the initial gas-phase C/O ratio is high.

The observed fractional abundances of NH₃ and CCS at the center of L1495A-N and L1521D correspond to chemical ages between 0.2 and 0.4 Myr using the mid-density model, which gives the modeled abundances of 4×10^{-9} for NH₃ and 2×10^{-10} for CCS. Table 3 shows the major reaction channels for production and destruction of NH₃, CCS, and HC₇N at the age

between 0.2 and 0.4 Myr for core outskirts and mid-density core model. If we use the high-density model, we have a chemical age matching the observed NH_3 abundance around 0.01 Myr. The high-density model results in younger ages because of the low abundance of CCS after 0.03 Myr. Considering that we have average densities of $(0.5\text{--}2) \times 10^5 \text{ cm}^{-3}$ toward the core centers of L1495A-N and L1521D, we do not think that the two cores have central densities near to $5 \times 10^5 \text{ cm}^{-3}$. Also, we do not observe any central depletion of NH_3 in L1495A-N and very little depletion of NH_3 in L1521D (only 20% decrease of the NH_3 fractional abundance), whereas the high-density model shows an order of magnitude decrease of the NH_3 fractional abundance. The density is also unlikely to reach the central density of $5 \times 10^5 \text{ cm}^{-3}$ within <0.01 Myr because a dense core typically takes much longer than 0.01 Myr to reach central density $5 \times 10^5 \text{ cm}^{-3}$ (e.g., Gong & Ostriker 2009, 2011). Thus, chemical ages of L1495A-N and L1521D using the mid-density core model, 0.2–0.4 Myr, fit better to the observed quantities and are similar to the ages of other dense cores (e.g., Ward-Thompson et al. 2007; Brünken et al. 2014).

The observed fractional abundances of NH_3 and CCS at the outskirts/CCS peak-intensity position of L1495A-N and L1521D also show good agreement with the outskirts model at an age between 0.2 and 0.4 Myr, which gives NH_3 and CCS fractional abundances 6×10^{-10} and 2×10^{-9} , respectively. This age range is relatively consistent with the chemical age at the core centers of L1495A-N and L1521D and also similar to the chemical ages of the other starless cores in the L1495-B218 filaments 0.3 Myr or older.

The comparisons between observations and the chemical models suggest that most regions of the L1495-B218 filaments have likely formed in an environment with the initial C/O ratio in the gas around 0.35, which is close to the solar value (Le Gal et al. 2014). However, for the two starless cores L1495A-N and L1521D, we were not able to explain high abundance of CCS and HC_7N unless we adopt chemical models with higher initial gas-phase C/O ratio of ≥ 1 . Because most of the cores in the L1495-B218 filaments agree with the chemical model with a low initial C/O, the initial C/O ratio across the Taurus molecular cloud was likely homogeneous with a value close to solar. Therefore, it appears likely that L1495A-N and L1521D underwent different formation mechanism or different evolutionary path compared to the rest of the cores in the L1495-B218 filaments.

Although the physics of having a high initial gas-phase C/O ratio is out of the scope of this article, we suggest two possible mechanisms that could produce results similar to the chemical model with a high initial C/O ratio in the gas (e.g., Hincelin et al. 2011, and references therein). The first possible mechanism is that a core forms by a collision of filaments. Generally, the gas-phase C/O ratio varies significantly depending on the gas density, extinction, and age. At a molecular cloud clump density $>1000 \text{ cm}^{-3}$, a gas-phase C/O ratio can increase significantly after ~ 1 Myr because of oxygen depletion. Thus, if molecular filaments are older than ~ 1 Myr and the collision of the filaments triggers core formation, the resulting cores would form in a high C/O ratio environment and have bright CCS and HC_7N emission. The second possible mechanism is that a core forms in a low C/O ratio environment (similar to the solar value), spends a long time in a quasi-static stage, and collapses while accreting gas from surrounding filament materials. The aged filament gas would have a high C/O ratio in the gas, so the accreted gas on the surface of

the core may develop abundant CCS and HC_7N and can make bright CCS and HC_7N rings.

4.2. A Stellar Association/Cluster-forming Candidate: L1495A/B7N

L1495A/B7N is the hub and the most evolved region of the L1495-B218 filaments. Seventeen of 35 young stellar objects along the filaments are associated with L1495A/B7N. L1495A/B7N has the highest column density along the filament and is also the most massive filament. Our NH_3 survey shows that L1495A/B7N is a gravitationally unstable clump with two NH_3 intensity peaks in L1495A-S and two NH_3 intensity peaks in L1495A-N (Seo et al. 2015). CCS and HC_7N in L1495A-N are as bright as NH_3 because of recently condensed gas, but the intensity peaks are displaced from the NH_3 peak. HCN & HCO^+ 1–0 observations show strong blue asymmetric, self-absorbed profiles, which indicate converging motions. In addition, gas flows in ^{12}CO are connected with flows seen in CCS and NH_3 in the PPV space. L1495A-N is currently gravitationally accreting gas and is also being fed gas by a large-scale flow.

We compare L1495A-N with theoretical models of quasi-static collapse of dense cores (Larson 1969; Penston 1969; Foster & Chevalier 1993; Gong & Ostriker 2009; Seo et al. 2013) to have an idea whether the inward flows toward L1495A-N are mainly due to gravitational collapse or to large-scale colliding flows. The theoretical models evaluate the minimum and the maximum converging-motion speeds due to gravitational collapse for a given density concentration. We compare the converging flow speed and the dimensionless dense core radius ξ_{max} of L1495A-N with those of the theoretical models. The ξ_{max} of L1495A-N is approximately 8, which is estimated by taking the long axis of L1495A-N measured in Seo et al. (2015) and the mean density calculated by dividing the column density by the size of the long axis. The calculation shows that L1495A-N has a converging flow roughly seven times faster than the maximum converging-motion speed that the gravitational collapse of a dense core can have at ξ_{max} of 8. The converging flow speed of L1495A-N even exceeds the maximum converging-motion speed of gravitational collapse during the whole evolution that are predicted by the theoretical models ($< \text{Mach } 4$, Larson 1969; Penston 1969; Foster & Chevalier 1993). Also, the position of the fastest converging motion in L1495A-N does not match with the fastest infall layer in the theoretical models, which is very near the core center in the last stage of collapse. Thus, L1495A-N is collapsing with an exceptional speed and likely has its dynamics driven by large-scale inflows.

We estimate the star formation rate in L1495A-N considering gas fed by large-scale inflows. We use the inflow velocity of 0.8 km s^{-1} measured in HCO^+ 1–0. We take the lowest column density along the 5σ signal-to-noise ratio edge of CCS emission in our map ($N = 5 \times 10^{21} \text{ cm}^{-2}$) and the long axis of L1495A-N seen in CCS (0.7 pc). We assume a star formation efficiency of 30%, which is the average efficiency for dense structures in molecular clouds (André et al. 2014). Our estimate gives $16 M_{\odot}/\text{Myr}$. L1495A/B7N is already associated with multiple young stellar objects and is likely to keep making stars, forming a stellar association/cluster, unless large-scale inflows are disturbed by radiation pressure or outflows from protostars.

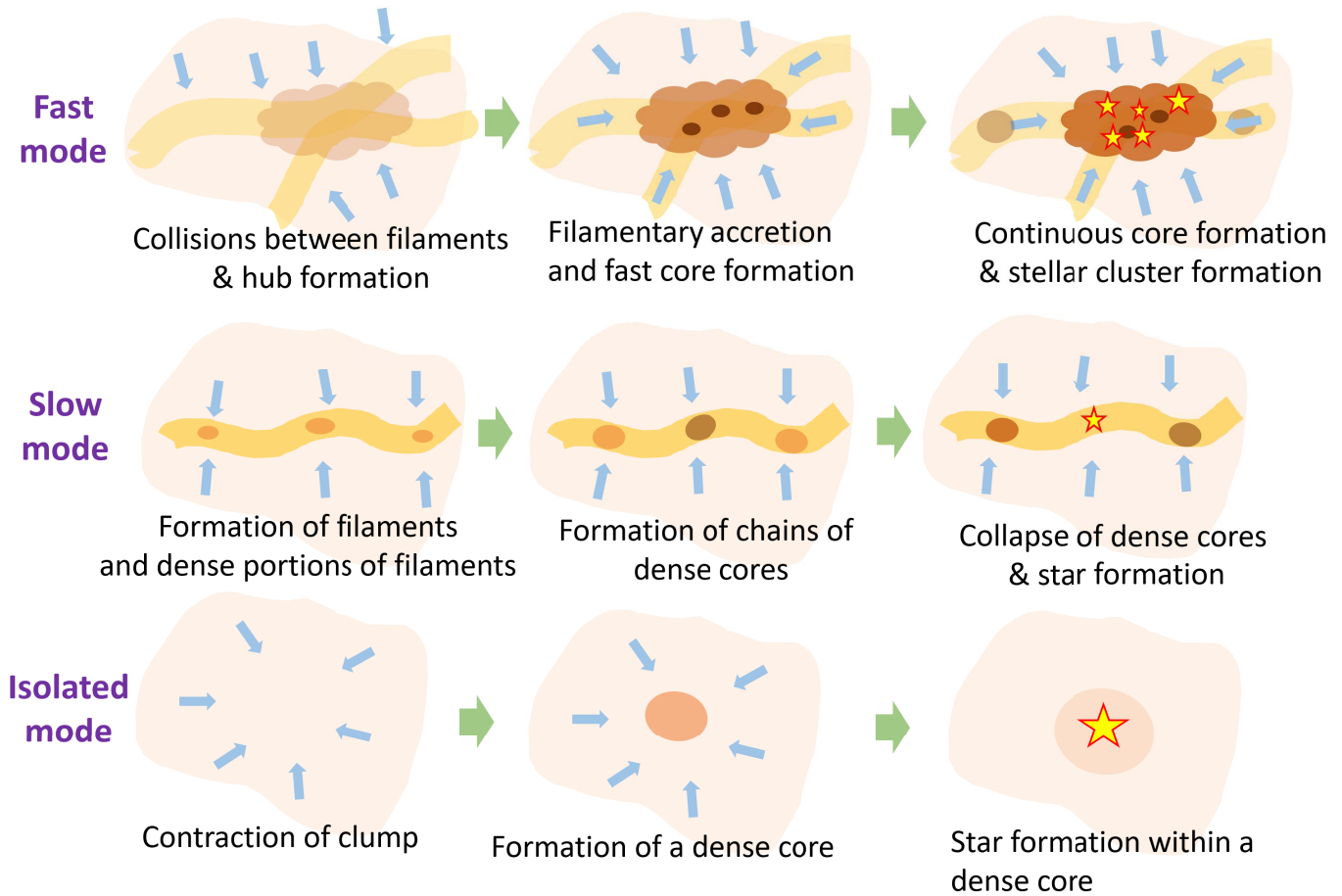


Figure 20. The three modes of star formation. The first (fast) mode describes star formation at the hub, where the column density is highest and the global gravitational potential well is deepest. Large-scale flows drive continuous star formation in relatively short time and form a stellar cluster/association. The second (slow) mode elaborates the formation of the dense core chains within filaments due to gravitational fragmentation of filaments and localized star formation within each core. The third (isolated) mode shows formation of an isolated dense core and localized star formation removed from filamentary structures, which is often discussed as conventional star formation (e.g., L1544, Bok globules).

4.3. Three Modes of Star Formation in the L1495-B218 Filaments and Implications to Low-mass Star Formation in Molecular Clouds

An important question in star formation within molecular cloud complexes is how the dynamical and chemical evolution in a cloud-scale structure are connected with and affect the small-scale dense structure in star formation. Through our new CCS, HC₇N, HCN, and HCO⁺ observations, along with observations in NH₃, CO isotopes, and far-infrared, we think that there may be three different star formation processes taking place in the L1495-B218 filaments (Figure 20): stellar cluster/association formation at the hub of filaments (fast mode), star formation in a chain of dense cores within a filament (slow mode), and star formation in an isolated dense core (isolated mode).

Analysis of the gas motions in the hub (L1495A/B7N) suggests that large-scale dynamics are playing a considerable role in not only forming dense cores but also collapsing dense cores and forming stars. The hub is the densest and the most massive part of the filaments and likely is formed through a collision of two or three filamentary structures. Observations in HCN, HCO⁺, and ¹³CO show that a large-scale converging flow (inferred from the blue asymmetry in HCN and HCO⁺ 1–0 and the velocity gradients along the three groups of

filaments) is still feeding the hub and driving collapse of cores. This ultimately promotes star formation because accreted gas adds more mass to dense cores, makes cores unstable, drives them to collapse, and also keeps forming new dense cores. Also, the ram pressure of a converging flow compresses dense cores to form protostars in a relatively short timescale (Gong & Ostriker 2009; Seo et al. 2013). Thus, in the hub, stars are expected to form fast and continuously unless the large-scale flows are disturbed, or the surrounding gas is depleted.

A chain of dense cores embedded within a filament (e.g., L1521D, No.30, No.31, and No.32 in B213E, which are not at the hub) is under the influence of surrounding filaments and neighboring dense cores, but their collapse may not be strongly related to their surroundings. The virial analysis of NH₃ dense cores within filaments shows that only some of the dense cores within filaments are gravitationally bound, whereas a number of the dense cores are pressure-confined within sterile filaments by the weight of the filament material surrounding dense cores and the ram pressure of a large-scale converging flow (Seo et al. 2015). Recent NH₃ surveys toward Orion A and Cepheus have also reported that there are a number of pressure-confined cores (Keown et al. 2017; Kirk et al. 2017). The denser portions of filaments likely grew as dense cores as the filaments gained more mass through accreting ambient gas or converging

flows of turbulent cells (Kirk et al. 2013; Palmeirim et al. 2013; Dhabal et al. 2018). Thus, the formation of dense cores is closely related with the formation and evolutionary history of the filaments. However, the subsequent collapse of dense cores does not seem to be directly related to the dynamics of filaments or to a large-scale flow in CO, as we show in L1521D. In this star formation process, the large-scale dynamics may have played a considerable role in forming filaments and dense cores but not in the final stage of forming a star within a dense core, which is similar to the *fray and fragment* model (Tafalla & Hacar 2015), except that we suggest a formation mechanism of the pressure-confined cores in sterile filaments in addition to the core formation through gravitational fragmentation of the molecular filaments (e.g., Schmalzl et al. 2010; Hacar & Tafalla 2011; Tafalla & Hacar 2015).

Finally, we found only one isolated dense core, core No.17, in the L1495-B218 filaments (Seo et al. 2015). It is not associated with any of the velocity-coherent filaments identified by Hacar et al. (2013) and also does not connect to the three groups of the filaments shown in Figure 11. Because it is detached from the filaments and its surroundings are ambient gas, it is not likely influenced by filaments or the large-scale dynamics of the filaments. Virial analysis of the core shows that it is in a marginally critical state and that its profile resembles the Bonnor–Ebert sphere, which are similar to characteristics found in other isolated cores and Bok globules (e.g., Bacmann et al. 2000; Kandori et al. 2005). This suggests that the core No.17 is evolving in a quasi-static manner in a relatively quiescent environment. The isolated mode has been studied using the brightest cores (e.g., L1544, Bok globules, and so forth); however, the recent Herschel surveys showed that that majority of dense cores are embedded within filaments (e.g., >60% in Aquila-Rift, André et al. 2010). Thus, the isolated mode is not likely a dominant mode of star formation in molecular clouds.

The three modes of star formation may also be found in other low-mass star-forming clouds. One of the examples with deep kinematic studies is Serpens-South. L1495A/B7N and the hub of Serpens-South share several similar characteristics, such as bright carbon-chain molecules including CCS and cyanopolyynes, along with bright NH₃ emission, an association of a stellar cluster, the signatures of colliding flows, and large-scale accretion toward the hub (Friesen et al. 2013; Kirk et al. 2013; Nakamura et al. 2014). The velocity gradients of large-scale flows seen in ¹²CO seem to be also similar between the two regions ($\sim 2 \text{ km s}^{-1} \text{ pc}^{-1}$) (Goldsmith et al. 2008; Tanaka et al. 2013). These characteristics strongly suggest that the hub of Serpens-South is also in the fast mode of star formation but in a scaled-up version compared to L1495A/B7N (L1495A/B7N: 0.7 pc, 60 M_{\odot} , 17 YSOs, Seo et al. 2015; Serpens-South: 10 pc, 360 M_{\odot} , 90 YSOs, Kirk et al. 2013). Within the filamentary regions of Serpens-South, there are small numbers of protostars with the fraction to the protostar population being much lower compared to the one at the hub, which is the same characteristic of the slow star formation mode in the L1495-B218 filaments in Taurus. Other than Serpens-South, the hub-filament structures in star-forming regions are very common across low-mass to high-mass star-forming regions (Myers 2009), and the fast mode or a similar star formation mode is often found to be the dominant processes in those regions (e.g., Serpens: Duarte-Cabral et al. 2010, 2011, OMC1-A: Hacar et al. 2017, G22: Yuan et al. 2018). Our study demonstrates that the Taurus

molecular cloud, which is relatively less active in star formation compared to Orion, infrared dark clouds, Serpens, and so forth, also has a similar mode of star formation, and might indicate an existence of a scalable star formation mode across star-forming regions.

The three modes of low-mass star formation may result in different initial mass functions (IMFs) of stars. The IMF is one of the most important properties of star formation because it determines the evolution of stellar clusters and galaxies and it has been extensively studied in both observation and theory to find realistic IMFs and to understand where it originates from. The clump mass function (CMF) is often studied to understand the origin of IMF (e.g., Offner et al. 2014), and some studies have reported that the CMF and the IMF share a similar form. However, on the basis of our study, the CMF may not be directly related to the origin of the IMF. The main contributors to the CMF are the chains of dense cores within the filaments. In the L1495-B218 filaments, 34 of 39 NH₃ cores are within the filaments, whereas we found only four NH₃ cores at the hub and one isolated dense core. For the IMF, on the other hand, the main contributors are protostars at the hub, because half of the protostars in the L1495-B218 filaments are associated with the hub, and more protostars are expected to form in the hub. This trend is also found in other molecular clouds. Myers (2013) showed multiple examples of hub structures in nearby molecular clouds and infrared dark clouds and demonstrated that these hub structures are associated with stellar groups or clusters. On the other hand, dense cores are typically not resolved because of the complexity of the hubs and observation limitations. It will be interesting to study how the different star formation modes affect the IMF.

5. Summary

In this article, we have presented CCS and HC₇N maps of the L1495-B218 filaments in the Taurus molecular cloud with an angular resolution of 31'' and a velocity resolution of 0.038 km s⁻¹. Using the maps, we investigated the chemistry and kinematics of the star-forming regions L1495A/B7N and B213E by comparing CCS and HC₇N to NH₃, 500 μm dust continuum, ¹²CO, and C¹⁸O. The main results are as follows:

1. We performed a complete survey in CCS and HC₇N along the L1495-B218 filament at noise levels of 120 mK for HC₇N $J = 21-20$ and 154 mK for CCS $J_N = 2_1-1_0$. We found strong CCS emission (>1 K) toward two more-evolved regions, L1495A/B7N and B213E, and one less-evolved region, B216. We observed weak CCS emission (<1 K) in a more-evolved region, B218, and a less-evolved region, B211. We found no detectable CCS emission in B10 and B213W at our noise level. Our survey shows that CCS emission is not related to the global evolutionary stages of regions.
2. CCS intensity peaks are not coincident with NH₃ and dust intensity peaks in most of the dense cores. Only in NH₃ core No.32 CCS, NH₃, and 500 μm dust continuum intensity peaks coincide in position. CCS emission in more-evolved regions, L1495A/B7N and B213E, shows an arclike or a ringlike shape. L1521B (in B216), which was previously reported to be a young CCS-bright core, also does not have CCS emission that coincides with the NH₃ or dust continuum emission peaks. These examples show that CCS rarely traces core structure.

3. We found through a grid of chemical models that the fractional abundance of CCS and HC₇N are significantly sensitive to the initial C/O ratio in the gas. In the model with the initial gas-phase C/O ratio being 0.35, which is close to the solar value, the evolution of the fractional abundances of CCS and HC₇N is similar to the chemical evolution shown in Suzuki et al. (1992) and Aikawa et al. (2001), where CCS and HC₇N are relatively abundant at a young age (<0.1 Myr) but get destroyed at later times (>0.5 Myr). On the other hand, when the initial C/O ratio in the gas is high (≥ 1), CCS and HC₇N are abundant for a long time. This suggests that CCS and HC₇N may be good tracers to constrain the initial C/O ratio in the gas rather than the evolutionary stage of dense cores. A future survey including multiple star-forming regions is required to confirm a correlation between the CCS and HC₇N fractional abundances and the initial gas-phase C/O ratio.
4. The velocity dispersions of CCS lines range from 0.15 to 0.3 km s⁻¹ with the majority of CCS spectra (94%) having velocity dispersion less than the average sound speed of the L1495-B213 filaments (0.19 km s⁻¹). Considering the large molecular weight of CCS and relatively small thermal velocity (0.04 km s⁻¹ at 10 K), this suggests that nonthermal motions in CCS-bright regions are subsonic, which is the same conclusion we obtained from our NH₃ survey. The transition-to-coherence is not observed at the sensitivity level of our observations.
5. L1495A/B7N is likely a stellar association/cluster-forming candidate. From the kinematics and chemistry of NH₃, CCS, ¹²CO, HCN, and HCO⁺, we find a supersonic converging flow toward L1495A-N and that is connected to a large-scale flow (>1 pc) seen in ¹³CO. L1495A/B7N is already associated with multiple protostars and is likely to form more protostars because of the converging flow. This may lead to formation of a stellar association or cluster in the region.
6. L1521D is a slowly contracting dense core. The converging motion is not connected with a large-scale flow seen in ¹²CO. Its converging-motion speed is subsonic, which is consistent with a spontaneous collapse model due to self-gravity.



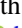

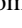




Finally, comparing the star formation processes in L1495A-N, L1521D, and isolated dense cores, we conclude that there are three different star formation modes in the L1495-B218 filaments. The first (fast) mode is star formation at the hub driven by a large-scale flow (e.g., L1495A/B7N) from the formation of filaments and dense cores to the collapse of dense cores. The second (slow) mode is the slow collapse of dense cores within filaments (e.g., L1521D). The third (isolated) mode is star formation through the quasi-static collapse of isolated starless cores (e.g., core No.17). Because other low-mass star-forming clouds share similar characteristics (hub-filament and isolated dense cores), the three processes are likely to be found in other molecular clouds as well. It will be important to study how each mode affects the evolution of molecular clouds and IMF of protostars and which is the dominant process in other molecular clouds.

We thank the anonymous referee for providing constructive comments that have improved the contents of this article. This research was performed in part at the Jet Propulsion Laboratory, California Institute of Technology, under a

contract with the National Aeronautics and Space Administration. We thank Hugo Medrano for his contributions to Argus. Y.S. and Y.L.S. were partially supported by NSF grant No. AST-1410190. Y.S. and L.M. acknowledges support from the NASA postdoctoral program.

Software: CLASS (Pety 2005), GBTIDL (Marganian et al. 2006), NAUTILUS (Ruaud et al. 2016).

ORCID iDs

Young Min Seo  <https://orcid.org/0000-0003-2122-2617>
 Liton Majumdar  <https://orcid.org/0000-0001-7031-8039>
 Paul F. Goldsmith  <https://orcid.org/0000-0002-6622-8396>
 Karen Willacy  <https://orcid.org/0000-0001-6124-5974>
 Derek Ward-Thompson  <https://orcid.org/0000-0003-1140-2761>
 Rachel Friesen  <https://orcid.org/0000-0001-7594-8128>
 David Frayer  <https://orcid.org/0000-0003-1924-1122>
 Dongwoo Chung  <https://orcid.org/0000-0003-2618-6504>
 Andrew I. Harris  <https://orcid.org/0000-0001-6159-9174>

References

- Agúndez, M., & Wakelam, V. 2013, *ChRv*, **113**, 8710
 Aikawa, Y., Ohashi, N., Inutsuka, S.-i., Herbst, E., & Takakuwa, S. 2001, *ApJ*, **552**, 639
 André, P., Di Francesco, J., Ward-Thompson, D., et al. 2014, in *Protostars and Planets VI*, ed. H. Beuther et al. (Tucson, AZ: Univ. Arizona Press), 27
 André, P., Men'shchikov, A., Bontemps, S., et al. 2010, *A&A*, **518**, L102
 Bacmann, A., André, P., Puget, J.-L., et al. 2000, *A&A*, **361**, 555
 Benson, P. J., Caselli, P., & Myers, P. C. 1998, *ApJ*, **506**, 743
 Bonnor, W. B. 1956, *MNRAS*, **116**, 351
 Brünken, S., Sipilä, O., Chambers, E. T., et al. 2014, *Natur*, **516**, 219
 Burge, C. A., Van Loo, S., Falle, S. A. E. G., & Hartquist, T. W. 2016, *A&A*, **596**, A28
 Campbell, J. L., Friesen, R. K., Martin, P. G., et al. 2016, *ApJ*, **819**, 143
 Cartledge, S. I. B., Lauroesch, J. T., Meyer, D. M., & Sofia, U. J. 2004, *ApJ*, **613**, 1037
 de Gregorio-Monsalvo, I., Gómez, J. F., Suárez, O., et al. 2006, *ApJ*, **642**, 319
 De Vries, C. H., & Myers, P. C. 2005, *ApJ*, **620**, 800
 Devaraj, K., Church, S., Cleary, K., et al. 2015, abstract in 2015 1st URSI Atlantic Radio Science Conf. (URSI AT-RASC)
 Dhabal, A., Mundy, L. G., Rizzo, M. J., Storm, S., & Teuben, P. 2018, *ApJ*, **853**, 169
 Dirienzo, W. J., Brogan, C., Indebetouw, R., et al. 2015, *AJ*, **150**, 159
 Duarte-Cabral, A., Dobbs, C. L., Peretto, N., & Fuller, G. A. 2011, *A&A*, **528**, A50
 Duarte-Cabral, A., Fuller, G. A., Peretto, N., et al. 2010, *A&A*, **519**, A27
 Ebert, R. 1955, *ZAp*, **37**, 217
 Ford, A. B., & Shirley, Y. L. 2011, *ApJ*, **728**, 144
 Foster, J. B., Rosolowsky, E. W., Kauffmann, J., et al. 2009, *ApJ*, **696**, 298
 Foster, P. N., & Chevalier, R. A. 1993, *ApJ*, **416**, 303
 Friesen, R. K., Medeiros, L., Schnee, S., et al. 2013, *MNRAS*, **436**, 1513
 Garrod, R. T. 2008, *A&A*, **491**, 239
 Goldsmith, P. F., Heyer, M., Narayanan, G., et al. 2008, *ApJ*, **680**, 428
 Gong, H., & Ostriker, E. C. 2009, *ApJ*, **699**, 230
 Gong, H., & Ostriker, E. C. 2011, *ApJ*, **729**, 120
 Goodman, A. A., Benson, P. J., Fuller, G. A., & Myers, P. C. 1993, *ApJ*, **406**, 528
 Graedel, T. E., Langer, W. D., & Frerking, M. A. 1982, *ApJS*, **48**, 321
 Hacar, A., Alves, J., Tafalla, M., & Goicoechea, J. R. 2017, *A&A*, **602**, L2
 Hacar, A., & Tafalla, M. 2011, *A&A*, **533**, A34
 Hacar, A., Tafalla, M., Kauffmann, J., & Kovács, A. 2013, *A&A*, **554**, A55
 Hincelin, U., Wakelam, V., Hersant, F., et al. 2011, *A&A*, **530**, A61
 Hirota, T., Ito, T., & Yamamoto, S. 2002, *ApJ*, **565**, 359
 Hirota, T., Maezawa, H., & Yamamoto, S. 2004, *ApJ*, **617**, 399
 Hirota, T., Ohishi, M., & Yamamoto, S. 2009, *ApJ*, **699**, 585
 Kandori, R., Nakajima, Y., Tamura, M., et al. 2005, *AJ*, **130**, 2166
 Keown, J., Di Francesco, J., Kirk, H., et al. 2017, *ApJ*, **850**, 3
 Kirk, H., Myers, P. C., Bourke, T. L., et al. 2013, *ApJ*, **766**, 115
 Kirk, H., Friesen, R. K., Pineda, J. E., et al. 2017, *ApJ*, **846**, 144
 Kirk, J. M., Crutcher, R. M., & Ward-Thompson, D. 2009, *ApJ*, **701**, 1044

- Larson, R. B. 1969, *MNRAS*, **145**, 271
- Le Bourlot, J., Pineau des Forets, G., Roueff, E., & Flower, D. R. 1995, *A&A*, **302**, 870
- Le Gal, R., Hily-Blant, P., Faure, A., et al. 2014, *A&A*, **562**, A83
- Lee, C. W., Myers, P. C., & Tafalla, M. 1999, *ApJ*, **526**, 788
- Lee, J.-E., Evans, N. J., II, Shirley, Y. L., & Tatematsu, K. 2003, *ApJ*, **583**, 789
- Loinard, L., Torres, R. M., Mioduszewski, A. J., et al. 2007, *ApJ*, **671**, 546
- Majumdar, L., Gratier, P., Andron, I., Wakelam, V., & Caux, E. 2017a, *MNRAS*, **467**, 3525
- Majumdar, L., Gratier, P., Wakelam, V., et al. 2018a, *MNRAS*, **477**, 525
- Majumdar, L., Loison, J.-C., Ruaud, M., et al. 2018b, *MNRAS*, **473**, L59
- Majumdar, L., Gratier, P., Ruaud, M., et al. 2017b, *MNRAS*, **466**, 4470
- Marganian, P., Garwood, R. W., Braatz, J. A., Radziwill, N. M., & Maddalena, R. J. 2006, in ASP Conf. Ser. 351, *Astronomical Data Analysis Software and Systems XV*, ed. C. Gabriel et al. (San Francisco, CA: ASP), 512
- Marka, C., Schreyer, K., Launhardt, R., Semenov, D. A., & Henning, T. 2012, *A&A*, **537**, A4
- Myers, P. C. 2005, *ApJ*, **623**, 280
- Myers, P. C. 2009, *ApJ*, **700**, 1609
- Myers, P. C. 2013, *ApJ*, **764**, 140
- Myers, P. C., Mardones, D., Tafalla, M., Williams, J. P., & Wilner, D. J. 1996, *ApJL*, **465**, L133
- Nakamura, F., Sugitani, K., Tanaka, T., et al. 2014, *ApJL*, **791**, L23
- Narayanan, G., Heyer, M. H., Brunt, C., et al. 2008, *ApJS*, **177**, 341
- Offner, S. S. R., Clark, P. C., Hennebelle, P., et al. 2014, in *Protostars and Planets VI*, ed. H. Beuther et al. (Tucson, AZ: Univ. Arizona Press), 53
- Ostriker, J. 1964, *ApJ*, **140**, 1056
- Pagani, L., Pardo, J.-R., Apponi, A. J., Bacmann, A., & Cabrit, S. 2005, *A&A*, **429**, 181
- Palmeirim, P., André, P., Kirk, J., et al. 2013, *A&A*, **550**, A38
- Penston, M. V. 1969, *MNRAS*, **145**, 457
- Pety, J. 2005, in SF2A-2005: Semaine de l'Astrophysique Française, ed. F. Casoli et al. (Les Ulis: EDP Sciences), 721
- Rathborne, J. M., Lada, C. J., Muench, A. A., Alves, J. F., & Lombardi, M. 2008, *ApJS*, **174**, 396
- Rebull, L. M., Padgett, D. L., McCabe, C.-E., et al. 2010, *ApJS*, **186**, 259
- Rebull, L. M., Koenig, X. P., Padgett, D. L., et al. 2011, *ApJS*, **196**, 4
- Rosolowsky, E. W., Pineda, J. E., Foster, J. B., et al. 2008, *ApJS*, **175**, 509
- Roy, N., Datta, A., Momjian, E., & Sarma, A. P. 2011, *ApJL*, **739**, L4
- Ruaud, M., Wakelam, V., & Hersant, F. 2016, *MNRAS*, **459**, 3756
- Scappini, F., Codella, C., & Guarnieri, A. 1996, *MNRAS*, **283**, L7
- Schmalzl, M., Kainulainen, J., Quanz, S. P., et al. 2010, *ApJ*, **725**, 1327
- Seo, Y. M., Hong, S. S., & Shirley, Y. L. 2013, *ApJ*, **769**, 50
- Seo, Y. M., Shirley, Y. L., Goldsmith, P., et al. 2015, *ApJ*, **805**, 185
- Shematovich, V. I., Wiebe, D. S., Shustov, B. M., & Li, Z.-Y. 2003, *ApJ*, **588**, 894
- Sieth, M., Devaraj, K., Voll, P., et al. 2014, *Proc. SPIE*, **9153**, 91530P
- Sohn, J., Lee, C. W., Park, Y.-S., et al. 2007, *ApJ*, **664**, 928
- Suzuki, H., Yamamoto, S., Ohishi, M., et al. 1992, *ApJ*, **392**, 551
- Tafalla, M., & Hacar, A. 2015, *A&A*, **574**, A104
- Tafalla, M., & Santiago, J. 2004, *A&A*, **414**, L53
- Tanaka, T., Nakamura, F., Awazu, Y., et al. 2013, *ApJ*, **778**, 34
- Tatematsu, K., Ohashi, S., Umemoto, T., et al. 2014a, *PASJ*, **66**, 16
- Tatematsu, K., Hirota, T., Ohashi, S., et al. 2014b, *ApJ*, **789**, 83
- Torres, R. M., Loinard, L., Mioduszewski, A. J., & Rodríguez, L. F. 2009, *ApJ*, **698**, 242
- van Dishoeck, E. F., & Blake, G. A. 1998, *ARA&A*, **36**, 317
- Vastel, C., Quéward, D., Le Gal, R., et al. 2018, *MNRAS*, **478**, 5514
- Vidal, T. H. G., Loison, J.-C., Jaziri, A. Y., et al. 2017, *MNRAS*, **469**, 435
- Vidal, T. H. G., & Wakelam, V. 2018, *MNRAS*, **474**, 5575
- Wakelam, V., Ruaud, M., Hersant, F., et al. 2016, *A&A*, **594**, A35
- Wakelam, V., Loison, J.-C., Herbst, E., et al. 2015, *ApJS*, **217**, 20
- Ward-Thompson, D., André, P., Crutcher, R., et al. 2007, in *Protostars and Planets V*, ed. B. Reipurth, D. Jewitt, & K. Keil (Tucson, AZ: Univ. Arizona Press), 33
- Williams, J. P., Lee, C. W., & Myers, P. C. 2006, *ApJ*, **636**, 952
- Wolkovitch, D., Langer, W. D., Goldsmith, P. F., & Heyer, M. 1997, *ApJ*, **477**, 241
- Yamamoto, S., Saito, S., Kawaguchi, K., et al. 1990, *ApJ*, **361**, 318
- Young, K. E., Lee, J.-E., Evans, N. J., II, Goldsmith, P. F., & Doty, S. D. 2004, *ApJ*, **614**, 252
- Yuan, J., Li, J.-Z., Wu, Y., et al. 2018, *ApJ*, **852**, 12